

Quantum Multicriticality in Disordered Weyl Semimetal

Xunlong Luo,^{1,2} Baolong Xu,^{1,2} Tomi Ohtsuki,³ and Ryuichi Shindou^{1,2,*}

¹*International Center for Quantum Materials, Peking University, Beijing 100871, China*

²*Collaborative Innovation Center of Quantum Matter, Beijing 100871, China*

³*Department of Physics, Sophia University, Chiyoda-ku, Tokyo 102-8554, Japan*

(Dated: April 6, 2024)

In electronic band structure of solid state material, two band touching points with linear dispersion appear in pair in the momentum space. When they annihilate with each other, the system undergoes a quantum phase transition from three-dimensional Weyl semimetal (WSM) phase to a band insulator phase such as Chern band insulator (CI) phase. The phase transition is described by a new critical theory with a ‘magnetic dipole’ like object in the momentum space. In this paper, we reveal that the critical theory hosts a novel disorder-driven quantum multicritical point, which is encompassed by three quantum phases, renormalized WSM phase, CI phase, and diffusive metal (DM) phase. Based on the renormalization group argument, we first clarify scaling properties around the band touching points at the quantum multicritical point as well as all phase boundaries among these three phases. Based on numerical calculations of localization length, density of states and critical conductance distribution, we next prove that a localization-delocalization transition between the CI phase with a finite zero-energy density of states (zDOS) and DM phase belongs to an ordinary 3D unitary class. Meanwhile, a localization-delocalization transition between the Chern insulator phase with zero zDOS and a renormalized Weyl semimetal (WSM) phase turns out to be a direct phase transition whose critical exponent $\nu = 0.80 \pm 0.01$. We interpret these numerical results by a renormalization group analysis on the critical theory.

I. INTRODUCTION

Novel quantum matters called Weyl semimetal [1, 2] have been recently discovered in a number of experimental materials [3–6], which show non-trivial magnetotransport properties [7–9] as a consequence of the chiral anomaly in 3+1 dimension. Besides its magnetotransport property, a Weyl semimetal with a linearly dispersive band-touching point (‘Weyl’ node) exhibits an intriguing quantum phase transition in the presence of moderate disorder strength; a quantum phase transition between renormalized Weyl semimetal (WSM) and diffusive metallic (DM) phases [10–32]. To clarify a critical nature of this quantum phase transition, scaling properties of density of states (DOS) around the Weyl node [10, 12, 15, 20–22, 25, 27, 31] and zero-energy conductivity [15, 21, 25] as well as their interplay with rare-event states [17, 30] have been extensively discussed.

The celebrated Nielsen-Ninomiya theorem dictates that single Weyl node cannot exist by itself in the momentum space of solid state material. Instead, two Weyl nodes with opposite magnetic charges always appear in pair in the first Brillouin zone. When a pair of the two nodes annihilate with each other in the momentum space, the system undergoes a quantum phase transition from WSM phase to a three-dimensional Chern band insulator (CI) phase. The quantum phase transition between these two phases is described by a new critical theory, which

we call in this paper as a “magnetic dipole” model,

$$\mathcal{H}_{\text{eff}} = \int d^2\mathbf{x}_{\perp} dx_3 \psi^{\dagger}(\mathbf{x}) \left\{ -iv(\partial_1\sigma_1 + \partial_2\sigma_2) + ((-i)^2 b_2 \partial_3^2 - m)\sigma_3 \right\} \psi(\mathbf{x}), \quad (1)$$

with $\mathbf{x}_{\perp} \equiv (x_1, x_2)$. σ_{μ} are 2 by 2 Pauli matrices ($\mu = 1, 2, 3$) and $\psi(\mathbf{x})$ denotes a two-component slowly-varying fermion field. A mass term (m) separates the WSM phase ($m > 0$) from the CI phase ($m < 0$). For $m < 0$, the effective Hamiltonian has a finite energy gap (CI phase). For $m > 0$, the Hamiltonian has a pair of the Weyl points in the momentum space, $(p_1, p_2, p_3) = (0, 0, \pm\sqrt{m/b_2})$. At the massless point ($m = 0$), the model supports a linearly dispersive energy band within a plane that is subtended by coordinates x_1 and x_2 , and a quadratic dispersion along a dipole direction (along the coordinate x_3). A tree-level renormalization group argument dictates that the critical phase at the massless point is robust against an infinitesimally small randomness (disorder), and persists up to a certain critical disorder strength. This suggests the presence of a new type of disorder-driven quantum phase transition between the critical phase near the clean limit and a DM phase above the critical disorder strength.

In this paper, we reveal that critical natures of this new type of the quantum phase transition is controlled by a novel quantum multicritical point (QMCP), from which three quantum phase boundaries are branching out; WSM-CI, WSM-DM, and CI-DM phase boundaries. Using a renormalization-group (RG) scaling argument, we first clarify unconventional DOS and conductivity scalings at Weyl nodes around QMCP as well as their crossover behavior among different critical regimes. We especially show that, around a quantum critical line be-

* rshindou@pku.edu.cn

tween WSM and CI phases as well as QMCP, the conductivity and diffusion constant along the in-plane direction and those along the dipole direction follows different universal scaling functions with different exponents! For the phase boundary between CI and DM phases, we numerically prove that a mobility edge and a band edge (red and yellow curves in Fig. 1, respectively) are distinct in the phase diagram, dictating the presence of a CI phase with finite zero-energy density of states (zDOS). A localization-delocalization transition between the CI with finite zDOS and DM phase belongs to the ordinary 3D unitary class [33–38]. Around a transition point between CI with zero zDOS and CI with finite zDOS, DOS for different disorder strengths and single-particle energies are well fitted into a single universal scaling function. Both critical exponent and dynamical exponent associated with this universal function are evaluated to be around one, respectively. For the phase boundary between CI and WSM phases, we numerically confirm that the transition between these two is direct. The associated critical exponent ν is estimated as 0.80 [0.79,0.81] by the localization length calculation. We interpret these results from a viewpoint of renormalization group analyses for a disordered magnetic-dipole model.

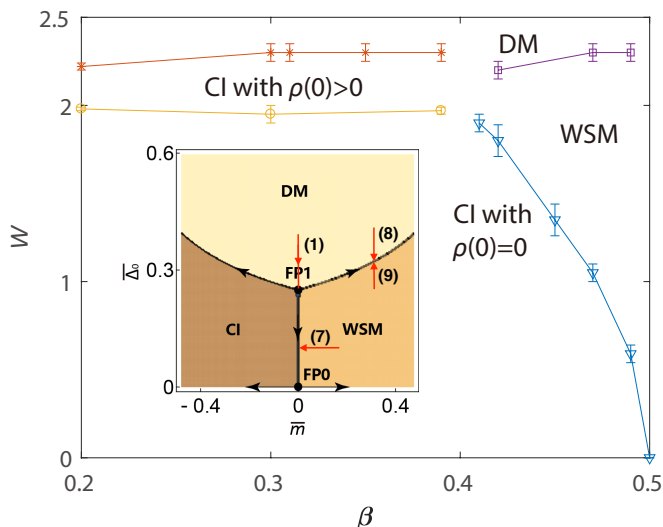


FIG. 1. (color online) Phase diagram for disordered Weyl semimetal. The horizontal axis indicates the coupling between the layers, while the vertical axis indicates the strength of disorder. Red, purple and blue lines are boundaries between CI and DM, between WSM and DM and between CI and WSM, respectively. These boundaries are determined by the localization length calculation. Yellow line is a boundary between CI phase with zero zero-energy density of states (zDOS) and CI phase with finite zDOS, which is determined by the density of states calculation. Inset: Phase diagram determined by perturbative renormalization group analyses (Ref. [31]. See also Appendix B of this paper). Red lines with arrow and number ((1), (7), (8), (9)) describe how the system approaches the critical lines or critical point in those cases that are considered in Table I.

II. LATTICE MODEL, MAGNETIC DIPOLE MODEL AND MULTICRITICAL QUANTUM PHASE TRANSITION

Let us first introduce a lattice model which supports the magnetic dipole model as its low-energy effective electronic Hamiltonian. In this paper, we numerically study a two-orbital tight-binding model on a cubic lattice [24–27]. The model is a layered Chern insulator (LCI), which consists of two-dimensional Chern insulator in the x_1 – x_2 plane with interlayer couplings along the x_3 -direction (see Appendix A). In the two-orbital model, we set a half electron filling (one band occupied, the other empty in the clean limit), and change an interlayer coupling strength (which we call β henceforth, see the Appendix A). When the coupling strength exceeds a critical value β_c , the two energy bands form pairs of linearly dispersive band-touching points (‘Weyl’ nodes) at the Fermi level. An electronic phase for $\beta > \beta_c$ is referred to as Weyl semimetal (WSM) phase, and a phase with an energy gap for $\beta < \beta_c$ as Chern band insulator (CI) phase. At the critical point, the low-energy effective electronic Hamiltonian takes the form of Eq. (1), where $\psi^\dagger(\mathbf{x})$ and $\psi(\mathbf{x})$ therein denote a two-component slowly-varying fermion field obtained from the $\mathbf{k}\cdot\mathbf{p}$ expansion around degenerate Weyl points at $\beta = \beta_c$. m corresponds to the interlayer coupling strength, $m = \beta - \beta_c$.

Effects of various types of disorders on the critical theory at the massless point of Eq. (1) can be captured by renormalization group (RG) analyses (Ref. [31] and Appendix B). A tree-level scaling argument dictates that a scaling dimension of the most relevant disorder is $-(d-5/2)$, where d is the spatial dimension, $d=3$. This suggests the presence of a non-trivial fixed point with a finite critical disorder strength, below which the disorder is irrelevant, while above which the disorder blows up to a larger value. A perturbative RG equation takes a form of coupled equations of the mass term m and properly normalized (chemical-potential type) disorder strength $\bar{\Delta}_0$;

$$\frac{dm}{dl} = m(1 - 2\bar{\Delta}_0), \quad (2)$$

$$\frac{d\bar{\Delta}_0}{dl} = -\frac{1}{2}\bar{\Delta}_0 + 2\bar{\Delta}_0^2, \quad (3)$$

with dl the scale change. The equation has a trivial fixed point in the clean limit $(\bar{\Delta}_0, m) = (0, 0)$ (FP0) and the nontrivial fixed point at finite critical disorder strength $(\bar{\Delta}_0, m) = (\Delta_c, 0)$ with $\Delta_c = 1/4$ (FP1). The critical phase described by Eq. (1) is stable up to the critical disorder strength $(\bar{\Delta}_0 < \Delta_c)$, above which a system enters a diffusive metallic (DM) phase $(\bar{\Delta}_0 > \Delta_c)$. The critical phase in $0 < \bar{\Delta}_0 < \Delta_c$ and $m = 0$ intervenes WSM and CI phases. The fixed point at $(\bar{\Delta}_0, m) = (\Delta_c, 0)$ plays role of a quantum multicritical point among WSM, CI and DM phases (inset of Fig. 1). In the phase diagram, there are three phase boundaries that branch out from the multicritical point. They are a boundary between CI and WSM phases, that between WSM and DM phases,

	$\rho(0)$ or $\rho(\mathcal{E})$	$\sigma_3(0)$ or $\sigma_3(\mathcal{E})$	$\sigma_\perp(0)$ or $\sigma_\perp(\mathcal{E})$
(1)	$\delta\bar{\Delta}_0 \frac{2d-1-2z}{2y_\Delta}$	$\delta\bar{\Delta}_0 \frac{2d-3}{2y_\Delta}$	$\delta\bar{\Delta}_0 \frac{2d-5}{2y_\Delta}$
(2)	$ \mathcal{E} ^{d-\frac{3}{2}}$	$ \mathcal{E} ^{d-\frac{3}{2}}$	$ \mathcal{E} ^{d-\frac{5}{2}}$
(3)	$ \delta\bar{\Delta}_0 ^{\frac{2d-1}{2}} \frac{1-z}{y_\Delta} \mathcal{E} ^{d-\frac{3}{2}}$	$ \delta\bar{\Delta}_0 ^{\frac{2d-3}{2}} \frac{1-z}{y_\Delta} \mathcal{E} ^{d-\frac{3}{2}}$	$ \delta\bar{\Delta}_0 ^{\frac{2d-5}{2}} \frac{1-z}{y_\Delta} \mathcal{E} ^{d-\frac{5}{2}}$
(4)	$ \mathcal{E} ^{\frac{d-z'}{z'}}$	$ \mathcal{E} ^{\frac{d-2}{z'}}$	same as σ_3
(5)	$m^{\frac{2d(z'-z)-z'}{2z'y_m}} \mathcal{E} ^{\frac{d-z'}{z'}}$	$m^{\frac{2d(z'-z)+4z-3z'}{2z'y_m}} \mathcal{E} ^{\frac{d-2}{z'}}$	$m^{\frac{2d(z'-z)+4z-5z'}{2z'y_m}} \mathcal{E} ^{\frac{d-2}{z'}}$
(6)	$ \mathcal{E} ^{\frac{2d-1-2z}{2z}}$	$ \mathcal{E} ^{\frac{2d-3}{2z}}$	$ \mathcal{E} ^{\frac{2d-5}{2z}}$
(7)	$m^{-\frac{1}{2}} \mathcal{E} ^{d-1}$	$m^{d-\frac{3}{2}}$	$m^{d-\frac{5}{2}}$
(8)	$\delta\bar{\Delta}_0 \frac{d-z'}{y_\Delta}$	$\delta\bar{\Delta}_0 \frac{d-2}{y_\Delta}$	same as σ_3
(9)	$ \delta\bar{\Delta}_0 ^{\frac{d-z'-d}{y_\Delta}} \mathcal{E} ^{d-1}$	$ \delta\bar{\Delta}_0 ^{\frac{d-2}{y_\Delta}}$	same as σ_3

TABLE I. Scalings of DOS and conductivities near Weyl nodes. \mathcal{E} denotes a single-particle energy. $\rho(0)$ and $\rho(\mathcal{E})$ are DOS for the zero-energy states and for finite (but small) energy states, respectively. $\sigma_\mu(0)$ and $\sigma_\mu(\mathcal{E})$ are the conductivities along the μ direction ($\mu = 3, \perp$) for the zero-energy and the finite energy states, respectively. The number such as (1), (7), (8), and (9) in the first column specifies a route along which the system approaches the quantum multicritical point ((1) or quantum critical lines ((7), (8), (9)). The routes with the same number are depicted as a red line with arrow in Fig. 1. In (2), (4) and (6), the system is on a quantum critical line between CI and WSM phases, on that between DM and WSM phases, and on the quantum multicritical point, respectively. In (3) and (5), the system approaches QMCP along (2) and (4). $\delta\bar{\Delta}_0$ denotes the disorder strength measured from a critical disorder strength of respective critical point (see also the text and Appendix). m denotes the mass term. y_Δ , y_m and z are scaling dimensions of the disorder strength $\delta\bar{\Delta}_0$, the mass term m , and the dynamical exponent at the quantum multicritical point (QMCP), respectively. y'_Δ and z' are scaling dimension of the disorder strength and dynamical exponent around a fixed point with finite disorder in disordered single Weyl node model respectively. See also Table IV in Appendix C.

and that between CI and DM phases. In the following section, we first employ the RG argument to clarify a rich variety of scaling properties of DOS, diffusion constant and conductivity around the quantum critical line between CI and WSM phases including the QMCP.

III. DOS AND CONDUCTIVITY SCALINGS AROUND QMCP

According to the RG equation, the critical properties of the quantum phase boundary between CI and WSM phases are controlled by the critical theory at the massless point of the magnetic dipole model (FP0). The theory has a quadratic dispersion along the dipole direction, and a linear dispersion along the in-plane direction. This naturally leads to a spatially anisotropic scaling around FP0;

$$x'_3 = b^{\frac{1}{2}} x_3, \quad (4)$$

$$x'_\perp = b x_\perp, \quad (5)$$

where $b \equiv e^{-dl} < 1$ counts how many times we carry out the renormalization; $-\ln b \equiv dl$ is same as dl in the left hand side of Eqs. (2) and (3). Here and henceforth, quantities with prime and quantities without prime denote those after the renormalization and before the renormalization, respectively. Under the anisotropic scaling, a volume is scaled by $b^{d-\frac{1}{2}}$. Thus, a total number of single-particle states below a given energy \mathcal{E} per unit volume $N(\mathcal{E}, \bar{\Delta}_0, m)$ is scaled by $b^{-(d-\frac{1}{2})}$ under the renormaliza-

tion;

$$N'(\mathcal{E}', \bar{\Delta}'_0, m') = b^{-(d-\frac{1}{2})} N(\mathcal{E}, \bar{\Delta}_0, m), \quad (6)$$

with $\mathcal{E}' = b^{-\bar{z}} \mathcal{E}$, $\bar{\Delta}'_0 = b^{-\bar{y}_\Delta} \bar{\Delta}_0$, and $m' = b^{-\bar{y}_m} m$. \bar{z} , \bar{y}_Δ and \bar{y}_m are dynamical exponent, scaling dimensions of the disorder strength $\bar{\Delta}_0$, and mass term m around the fixed point in the clean limit (FP0). In terms of the dynamical exponent, the density of states is scaled by $b^{-(d-\frac{1}{2}-\bar{z})}$ under the renormalization,

$$\rho'(\mathcal{E}', \bar{\Delta}'_0, m') = b^{-(d-\frac{1}{2}-\bar{z})} \rho(\mathcal{E}, \bar{\Delta}_0, m) \quad (7)$$

with $\rho(\mathcal{E}) \equiv dN(\mathcal{E})/d\mathcal{E}$. The critical theory in the clean limit has its dynamical exponent to be one; $\bar{z} = 1$. Around FP0, the disorder is an irrelevant scaling variable, $\bar{y}_\Delta = -(d - \frac{5}{2})$, while the mass term is a relevant scaling variable, $\bar{y}_m = 1$. To see how DOS near Weyl nodes is scaled by the single-particle energy near the quantum critical line between CI and WSM phases, we take m to be tiny and $\bar{\Delta}_0 < \Delta_c$. Let us renormalize the system many times, such that $m' = b^{-\bar{y}_m} m = 1$. Solving b in favor for small m , we reach,

$$\rho(\mathcal{E}, \bar{\Delta}_0, m) = m^{d-\frac{3}{2}} \rho'(m^{-1}\mathcal{E}, m^{-\bar{y}_\Delta} \bar{\Delta}_0, 1). \quad (8)$$

When m is tiny, the second argument in the right hand side can be replaced by zero, because $\bar{y}_\Delta < 0$. This leads to the following universal DOS scaling around the CI-WSM branch:

$$\rho(\mathcal{E}, \bar{\Delta}_0, m) = m^{d-\frac{3}{2}} \Phi(m^{-1}\mathcal{E}), \quad (9)$$

for small m and arbitrary $\bar{\Delta}_0 < \Delta_c$.

The anisotropic scaling in the magnetic dipole model also leads to unconventional scalings of the diffusion constant near Weyl nodes. To see this, we consider a mean square displacement of single-particle states of energy \mathcal{E} at a time s as a function of the two scaling variables:

$$g_3(\mathcal{E}, s, \bar{\Delta}_0, m) \equiv \langle x_3^2 \rangle(\mathcal{E}, s, \bar{\Delta}_0, m), \quad (10)$$

$$g_\perp(\mathcal{E}, s, \bar{\Delta}_0, m) \equiv \langle \mathbf{x}_\perp^2 \rangle(\mathcal{E}, s, \bar{\Delta}_0, m). \quad (11)$$

Under the scaling, the displacement along the dipole direction (g_3) and that along the in-plane direction (g_\perp) are scaled with different exponents;

$$b^{-1}g'_3(\mathcal{E}', s', \bar{\Delta}'_0, m') = g_3(\mathcal{E}, s, \bar{\Delta}_0, m), \quad (12)$$

$$b^{-2}g'_\perp(\mathcal{E}', s', \bar{\Delta}'_0, m') = g_\perp(\mathcal{E}, s, \bar{\Delta}_0, m), \quad (13)$$

and $s' = b^z s$ ($z = 1$). This leads to the following universal scaling forms of the mean square displacements,

$$g_3(\mathcal{E}, s, \bar{\Delta}_0, m) = m^{-1}\Psi_3(m^{-1}\mathcal{E}, ms), \quad (14)$$

$$g_\perp(\mathcal{E}, s, \bar{\Delta}_0, m) = m^{-2}\Psi_\perp(m^{-1}\mathcal{E}, ms), \quad (15)$$

for small m and arbitrary $\bar{\Delta}_0 < \Delta_c$. For small m , we may further expand the right hand side with respect to small ms for an arbitrary time s , to obtain the following universal scaling forms of the diffusion constants at Weyl nodes,

$$D_3(\mathcal{E}, \bar{\Delta}_0, m) = f_3(m^{-1}\mathcal{E}), \quad (16)$$

$$D_\perp(\mathcal{E}, \bar{\Delta}_0, m) = m^{-1}f_\perp(m^{-1}\mathcal{E}). \quad (17)$$

Here D_3 and D_\perp denote a diffusion constant along the dipole direction (x_3) and that within the in-plane direction (\mathbf{x}_\perp), respectively, which are linear coefficients of the mean square displacements in time s ; $g_\mu(\dots, s, \dots) = D_\mu(\dots)s + \mathcal{O}(s^2)$ ($\mu = 3, \perp$).

For finite positive m , the low-energy electronic band structure comprises of the pair of the two Weyl nodes. Thereby, we regard that, in the WSM phase, ($m > 0$ and $\bar{\Delta}_0 < \Delta_c$), $\rho(\mathcal{E}) \propto \mathcal{E}^{d-1}$ and $D_\mu(\mathcal{E}) \propto \mathcal{E}^{-(d-1)}$ for $\mathcal{E} < m$. When combined with Eqs. (9), (16), and (17), this requires

$$\begin{cases} \rho(\mathcal{E}, \bar{\Delta}_0, m) \propto m^{-\frac{1}{2}}\mathcal{E}^{d-1}, \\ D_3(\mathcal{E}, \bar{\Delta}_0, m) \propto m^{d-1}\mathcal{E}^{-(d-1)}, \\ D_\perp(\mathcal{E}, \bar{\Delta}_0, m) \propto m^{d-2}\mathcal{E}^{-(d-1)}, \\ \sigma_3(\mathcal{E}, \bar{\Delta}_0, m) \propto m^{d-\frac{3}{2}}, \\ \sigma_\perp(\mathcal{E}, \bar{\Delta}_0, m) \propto m^{d-\frac{5}{2}}, \end{cases} \quad (18)$$

for small m and arbitrary $\bar{\Delta}_0 < \Delta_c$. Here σ_3 and σ_\perp are conductivity along the dipole direction (x_3) and that within the in-plane direction (\mathbf{x}_\perp), that are related with diffusion constants and the density of states via the Einstein relation, $\sigma_\mu(\mathcal{E}) \equiv e^2\rho(\mathcal{E})D_\mu(\mathcal{E})$ ($\mu = 3, \perp$). At non-zero single-particle energy, both DOS and diffusion constants are finite even at the critical line ($m = 0$). When combined with Eqs. (9), (16), and (17), this tells how

DOS and diffusion constants as well as conductivities are scaled by the single-particle energy \mathcal{E} at $m = 0$,

$$\begin{cases} \rho(\mathcal{E}, \bar{\Delta}_0, m = 0) \propto \mathcal{E}^{d-\frac{3}{2}}, \\ D_3(\mathcal{E}, \bar{\Delta}_0, m = 0) \propto \mathcal{E}^0, \\ D_\perp(\mathcal{E}, \bar{\Delta}_0, m = 0) \propto \mathcal{E}^{-1}, \\ \sigma_3(\mathcal{E}, \bar{\Delta}_0, m = 0) \propto \mathcal{E}^{d-\frac{3}{2}}, \\ \sigma_\perp(\mathcal{E}, \bar{\Delta}_0, m = 0) \propto \mathcal{E}^{d-\frac{5}{2}}, \end{cases} \quad (19)$$

for arbitrary $\bar{\Delta}_0 < \Delta_c$.

According to the RG equations given by Eqs. (2) and (3), the scaling around QMCP (FP1) has two relevant scaling variables, $\delta\bar{\Delta}_0 \equiv \bar{\Delta}_0 - \Delta_c$ and the mass term m . Under the renormalization, DOS and mean square displacements are scaled as follows,

$$b^{d-\frac{1}{2}-z}\rho'(b^{-z}\mathcal{E}, b^{-y_\Delta}\delta\bar{\Delta}_0, b^{-y_m}m) = \rho(\mathcal{E}, \delta\bar{\Delta}_0, m),$$

$$b^{-1}g'_3(b^{-z}\mathcal{E}, b^z s, b^{-y_\Delta}\delta\bar{\Delta}_0, b^{-y_m}m) = g_3(\mathcal{E}, s, \delta\bar{\Delta}_0, m),$$

$$b^{-2}g'_\perp(b^{-z}\mathcal{E}, b^z s, b^{-y_\Delta}\delta\bar{\Delta}_0, b^{-y_m}m) = g_\perp(\mathcal{E}, s, \delta\bar{\Delta}_0, m),$$

where z , y_Δ and y_m are dynamical exponent, scaling dimensions of $\delta\bar{\Delta}_0$ and m around FP1. Within large- n RG analysis (see Ref. [31] and Appendix B), they are evaluated as $z = 1 + \frac{1}{n} + \mathcal{O}(n^{-2})$, $y_m = 1 - \frac{1}{n} + \mathcal{O}(n^{-2})$, and $y_\Delta = \frac{1}{n} + \mathcal{O}(n^{-2})$ with $n = 2$.

When the system approaches QMCP along $m = 0$, the DOS and diffusion constants near Weyl nodes respect the following universal scaling forms,

$$\rho(\mathcal{E}, \delta\bar{\Delta}_0, m = 0) = |\delta\bar{\Delta}_0|^{\frac{d-\frac{1}{2}-z}{y_\Delta}}\Psi(|\delta\bar{\Delta}_0|^{-\frac{z}{y_\Delta}}\mathcal{E}), \quad (20)$$

$$D_3(\mathcal{E}, \delta\bar{\Delta}_0, m = 0) = |\delta\bar{\Delta}_0|^{\frac{z-1}{y_\Delta}}f_z(|\delta\bar{\Delta}_0|^{-\frac{z}{y_\Delta}}\mathcal{E}), \quad (21)$$

$$D_\perp(\mathcal{E}, \delta\bar{\Delta}_0, m = 0) = |\delta\bar{\Delta}_0|^{\frac{z-2}{y_\Delta}}f_\perp(|\delta\bar{\Delta}_0|^{-\frac{z}{y_\Delta}}\mathcal{E}), \quad (22)$$

In the DM phase side ($\delta\bar{\Delta}_0 > 0$) with finite zero-energy DOS and diffusion constant, this leads to

$$\begin{cases} \rho(\mathcal{E} = 0, \delta\bar{\Delta}_0 > 0, m = 0) \propto |\delta\bar{\Delta}_0|^{\frac{d-\frac{1}{2}-z}{y_\Delta}}, \\ D_3(\mathcal{E} = 0, \delta\bar{\Delta}_0 > 0, m = 0) \propto |\delta\bar{\Delta}_0|^{\frac{z-1}{y_\Delta}}, \\ D_\perp(\mathcal{E} = 0, \delta\bar{\Delta}_0 > 0, m = 0) \propto |\delta\bar{\Delta}_0|^{\frac{z-2}{y_\Delta}}, \\ \sigma_3(\mathcal{E} = 0, \delta\bar{\Delta}_0 > 0, m = 0) \propto |\delta\bar{\Delta}_0|^{\frac{d-\frac{3}{2}}{y_\Delta}}, \\ \sigma_\perp(\mathcal{E} = 0, \delta\bar{\Delta}_0 > 0, m = 0) \propto |\delta\bar{\Delta}_0|^{\frac{d-\frac{5}{2}}{y_\Delta}}. \end{cases} \quad (23)$$

In the side of the quantum critical line between CI and WSM phases ($\delta\bar{\Delta}_0 < 0$), Eqs. (20), (21), and (22) in combination with Eq. (19) leads to,

$$\begin{cases} \rho(\mathcal{E}, \delta\bar{\Delta}_0 < 0, m = 0) \propto |\delta\bar{\Delta}_0|^{\frac{2d-1}{2}\frac{1-z}{y_\Delta}}\mathcal{E}^{d-\frac{3}{2}}, \\ D_3(\mathcal{E}, \delta\bar{\Delta}_0 < 0, m = 0) \propto |\delta\bar{\Delta}_0|^{\frac{z-1}{y_\Delta}}, \\ D_\perp(\mathcal{E}, \delta\bar{\Delta}_0 < 0, m = 0) \propto |\delta\bar{\Delta}_0|^{\frac{2(z-1)}{y_\Delta}}\mathcal{E}^{-1}, \\ \sigma_3(\mathcal{E}, \delta\bar{\Delta}_0 < 0, m = 0) \propto |\delta\bar{\Delta}_0|^{\frac{2d-3}{2}\frac{1-z}{y_\Delta}}\mathcal{E}^{d-\frac{3}{2}}, \\ \sigma_\perp(\mathcal{E}, \delta\bar{\Delta}_0 < 0, m = 0) \propto |\delta\bar{\Delta}_0|^{\frac{2d-5}{2}\frac{1-z}{y_\Delta}}\mathcal{E}^{d-\frac{5}{2}}. \end{cases} \quad (24)$$

When the system approaches QMCP along $\delta\bar{\Delta}_0 = 0$, the DOS and diffusion constants respect the following

universal scaling forms,

$$\rho(\mathcal{E}, \delta\bar{\Delta}_0 = 0, m) = |m|^{\frac{d-\frac{1}{2}-z}{y_m}} \Psi(|m|^{-\frac{z}{y_m}} \mathcal{E}), \quad (25)$$

$$D_3(\mathcal{E}, \delta\bar{\Delta}_0 = 0, m) = |m|^{\frac{z-1}{y_m}} f_z(|m|^{-\frac{z}{y_m}} \mathcal{E}), \quad (26)$$

$$D_{\perp}(\mathcal{E}, \delta\bar{\Delta}_0 = 0, m) = |m|^{\frac{z-2}{y_m}} f_{\perp}(|m|^{-\frac{z}{y_m}} \mathcal{E}). \quad (27)$$

In the side of the quantum critical line between DM and WSM phases ($m > 0$), the DOS and diffusion constant are scaled by finite small energy \mathcal{E} as

$$\rho(\mathcal{E}, \delta\bar{\Delta}_0 = 0, m > 0) \propto |\mathcal{E}|^{\frac{d-z'}{z'}}, \quad (28)$$

$$D_{\mu}(\mathcal{E}, \delta\bar{\Delta}_0 = 0, m > 0) \propto |\mathcal{E}|^{\frac{z'-2}{z'}}, \quad (29)$$

with $\mu = 3, \perp$ (see Ref. [15, 25] and Appendix). Here z' is dynamical exponent at the semimetal-metal quantum phase transition in disordered single Weyl node [10, 12, 15, 20–22, 25, 27]. This in combination with Eqs. (25), (26), and (27) gives

$$\left\{ \begin{array}{l} \rho(\mathcal{E}, \delta\bar{\Delta}_0 = 0, m > 0) \propto |m|^{\frac{2d(z'-z)-z'}{2z'y_m}} \mathcal{E}^{\frac{d-z'}{z'}}, \\ D_3(\mathcal{E}, \delta\bar{\Delta}_0 = 0, m > 0) \propto |m|^{\frac{2z-z'}{z'y_m}} \mathcal{E}^{\frac{z'-2}{z'}}, \\ D_{\perp}(\mathcal{E}, \delta\bar{\Delta}_0 = 0, m > 0) \propto |m|^{\frac{2(z-z')}{z'y_m}} \mathcal{E}^{\frac{z'-2}{z'}}, \\ \sigma_3(\mathcal{E}, \delta\bar{\Delta}_0 = 0, m > 0) \propto |m|^{\frac{2d(z'-z)+4z-3z'}{2z'y_m}} \mathcal{E}^{\frac{d-2}{z'}}, \\ \sigma_{\perp}(\mathcal{E}, \delta\bar{\Delta}_0 = 0, m > 0) \propto |m|^{\frac{2d(z'-z)+4z-5z'}{2z'y_m}} \mathcal{E}^{\frac{d-2}{z'}}, \end{array} \right. \quad (30)$$

for small positive m . On QMCP ($\delta\bar{\Delta}_0 = 0, m = 0$), DOS and diffusion constants are scaled by finite small energy \mathcal{E} as,

$$\left\{ \begin{array}{l} \rho(\mathcal{E}, \delta\bar{\Delta}_0 = 0, m = 0) = |\mathcal{E}|^{\frac{d-\frac{1}{2}-z}{z}}, \\ D_3(\mathcal{E}, \delta\bar{\Delta}_0 = 0, m = 0) = |\mathcal{E}|^{\frac{z-1}{z}}, \\ D_{\perp}(\mathcal{E}, \delta\bar{\Delta}_0 = 0, m = 0) = |\mathcal{E}|^{\frac{z-2}{z}}, \\ \sigma_3(\mathcal{E}, \delta\bar{\Delta}_0 = 0, m = 0) = |\mathcal{E}|^{\frac{d-\frac{3}{2}}{z}}, \\ \sigma_{\perp}(\mathcal{E}, \delta\bar{\Delta}_0 = 0, m = 0) = |\mathcal{E}|^{\frac{d-\frac{5}{2}}{z}}. \end{array} \right. \quad (31)$$

The DOS and conductivities scalings around QMCP as well as the quantum critical lines for CI-WSM branch and that for WSM-DM branch are summarized in Table I.

As for transition between CI and DM phases, a situation becomes more involved. Firstly, our numerical studies below reveal that, unlike in the WSM-DM phase boundary, a mobility edge and a band edge are distinct for the CI-DM phase boundary, indicating the presence of the CI phase with finite zero-energy density of states (zDOS). Let us call the CI phase with finite zDOS as CI' phase. In the following, we first show that localization-delocalization transition between the CI' phase and DM phase belongs to the ordinary 3D unitary class. In Sec. V, we show that, on increasing the disorder strength, the gapped Chern band insulator phase acquires a finite zDOS below the localization-delocalization transition.

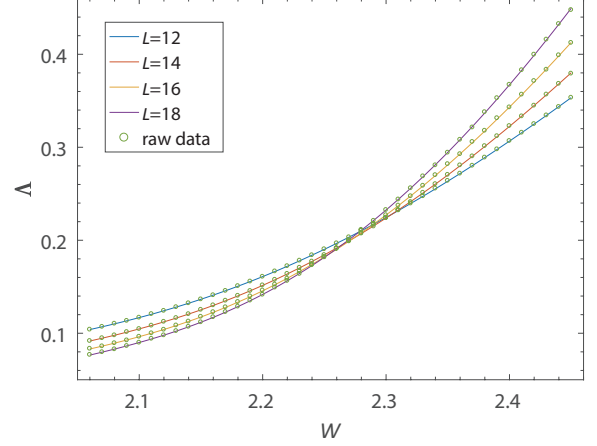


FIG. 2. (color online) $\Lambda \equiv \lambda/L$ as a function of disorder strength for $\beta = 0.2$ with a cross section size $L = 12, 14, 16, 18$. The circle is the raw data of Λ and the four curves are the fitting result with the Taylor-expansion orders: $(m_1, m_2, n_1, n_2) = (2, 0, 3, 1)$ (see the text).

m_1	m_2	GOF	W_c	ν	$-y$
2	0	0.27	2.21[2.19,2.23]	1.34[1.23,1.53]	2.6[2.0,3.4]
3	0	0.82	2.22[2.18,2.23]	1.27[1.18,1.48]	3.0[2.0,4.0]
2	1	0.29	2.22[2.19,2.23]	1.31[1.22,1.52]	3.0[2.1,3.9]
3	1	0.81	2.22[2.18,2.23]	1.26[1.18,1.48]	2.9[2.0,3.8]

TABLE II. Polynomial fitting results for the localization-delocalization transition between CI and DM phases at $\beta = 0.2$ with $(n_1, n_2) = (3, 1)$. The goodness of fit (GOF), critical disorder W_c , critical exponent $\nu \equiv 1/\alpha_1$, largest irrelevant exponent y are shown for different orders of the Taylor expansion (m_1, m_2) . A value of Λ at the critical point is 0.14 [0.11, 0.16]. Error bar in the square bracket denotes the 95% confidence interval.

IV. CRITICAL EXPONENT AND CRITICAL CONDUCTANCE FOR CI-DM BRANCH

To clarify the nature of the phase transition between CI and DM phases, we include in LCI a short-ranged on-site disorder potential, whose strength is denoted by W henceforth, and calculate a quasi-one dimensional localization length λ of eigenstates at the Fermi level ($E = 0$) by transfer matrix method. We use a quasi-one-dimensional geometry with a square cross-section $L_x = L_y = L$ in x_1-x_2 plane, to calculate the localization length along the x_3 -direction with variable length L_z . For longer L_z , smaller is the standard deviation σ_{Λ} of a normalized localization length $\Lambda \equiv \lambda/L$ [39, 40]. We terminate the transfer matrix calculation, when a precision σ_{Λ}/Λ reaches 0.1% for $L = 12, 14$ and 0.2 % for $L = 16, 18$. Fig. 2 shows Λ as a function of W for different L . The scale-invariant behavior of Λ indicates a localization-delocalization phase transition induced by W .

To determine a critical disorder strength W_c and crit-

ical exponent of the phase transition, we use polynomial fitting method. We assume that the normalized localization length Λ depends on disorder strength W and system size L through a universal function of only two scaling variables, $F(\phi_1, \phi_2)$ [41, 42]. ϕ_1 is a relevant scaling variable with positive exponent $\alpha_1 \equiv 1/\nu$ and ϕ_2 is an irrelevant scaling variable with the largest negative exponent $\alpha_2 \equiv y$. Λ depends on W and L through the scaling variables, $\phi_j \equiv u_j(\omega)L^{\alpha_j}$ where $\omega \equiv (W - W_c)/W_c$. By definition, $u_1(\omega = 0) = 0$ and $u_2(\omega = 0) \neq 0$. Assuming that ω is small and L is large enough, we Taylor-expand the universal function in small ϕ_1 and ϕ_2 and $u_j(\omega)$ in small ω ; $\Lambda = F(\phi_1, \phi_2) = \sum_{j_1=0}^{n_1} \sum_{j_2=0}^{n_2} a_{j_1, j_2} \phi_1^{j_1} \phi_2^{j_2}$, $u_i(\omega) = \sum_{j=0}^{m_i} b_{i, j} \omega^j$. For a given set of (n_1, n_2, m_1, m_2) , we minimize $\chi^2 \equiv \sum_{j=1}^{N_D} (F_j - \Lambda_j)^2 / \sigma_j^2$ in terms of W_c , $\alpha_1 \equiv \nu^{-1}$, $\alpha_2 \equiv y$, $a_{i, j}$, and $b_{l, m}$ with $a_{1,0} = a_{0,1} = 1$ and $b_{1,0} = 0$. Λ_j and σ_j ($j = 1, \dots, N_D$) are values of Λ and σ_Λ in Fig. 2 for a given L and W . j specifies a data point, while N_D is a number of those data points that are used for the fitting. F_j is a value of Λ from the polynomial fitting at the same L and W . Fittings are carried out for several different (n_1, n_2, m_1, m_2) with $n_1, n_2, m_1 \leq 3$, $m_2 \leq 2$. Those fitting results with goodness of fit (GOF) greater than 0.1 is shown in Table II. We also carry out the same fitting for 1000 synthetic data sets of $\{\Lambda_1, \dots, \Lambda_{N_D}\}$, to determine 95% confidence interval [42].

A fit with the smallest number of parameters gives the exponent $\nu = 1.34$ [1.23, 1.53]. The fitting is stable against the increase of the expansion orders (Table I and Appendix E). The value is consistent with $\nu_{3d,u} \approx 1.443$ [.437, .449] [35] for the ordinary 3D unitary class, suggesting that the localization-delocalization transition between CI and DM phases belong to the same universality class as the ordinary 3D unitary class [33–38].

To reinforce the above result, we calculate a critical conductance distribution (CCD) and compare this with CCD in a reference tight-binding model whose Anderson transition is known to belong to the ordinary 3D universality class [33]. CCD generally depends only on the symmetry class and system's geometry, but free from a system size [43]. The geometry of a system is determined by mean values of two-terminal conductance at the critical point along x_1 , x_2 and x_3 directions, i. e. G_x , G_y and G_z . In our model, $G_x = G_y \equiv G_\perp$, while out-plane conductance G_z differs from the in-plane conductance G_\perp . We fine-tune L_z with fixed $L_x = L_y = L$, such that G_z and G_\perp at the critical point become identical (very close) to those calculated from the reference tight-binding model [33]. For the critical point shown in Fig. 2, $L/L_z = 4$ realizes this. Fig. 3 shows a distribution of G_z at the critical point with different L with fixed $L/L_z = 4$. The distributions are almost identical to the CCD in the reference tight-binding model. This in combination with the critical exponent concludes that the localization-delocalization transition for the CI-DM

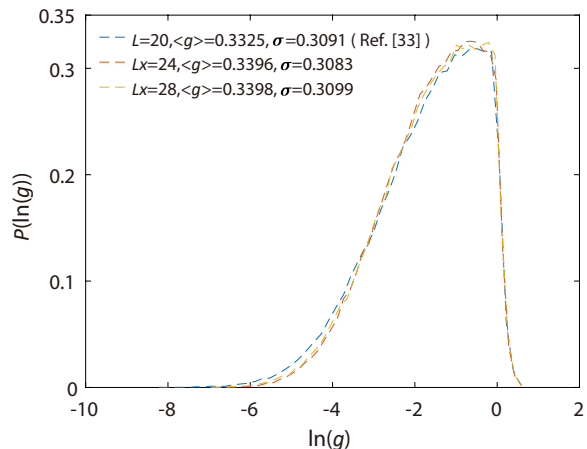


FIG. 3. (color online) Critical conductance distributions (CCD) along the x_3 -direction of LCI model at $W = W_c = 2.21, \beta = 0.2$ with $L_x = L_y = 4L_z$ (periodic boundary conditions in x_1 and x_2 directions). $L_x = 24$ (red broken line) and $L_x = 28$ (orange). CCD of the reference model (called as a cubic U(1) tight-binding model [33]) (blue) is compared with them. Each distribution include 10^5 samples. g is the two terminal conductance G_z in unit of e^2/h .

branch belong to the ordinary 3D unitary class.

V. DENSITY OF STATES FOR CI-DM BRANCH

The above observation indicates that, unlike in the critical line between DM and WSM phases [10–30], zDOS is finite at the localization-delocalization transition between DM and CI phases. To confirm this, we calculate DOS in disordered LCI with cubic geometry ($L_x = L_y = L_z = L$) by kernel polynomial expansion method [44]. We set L to be 100 and/or 200 and the order of the Chebyshev polynomial expansion to a few thousands. Considering a self-averaging nature of DOS, we average the calculated DOS over two ($L = 200$) and four ($L = 100$) different disorder realizations. On increasing the disorder strength W , we found that the gapped (Chern) band insulator phase acquires a finite zDOS $\rho(0)$ below the localization-delocalization transition point, $\rho(0) \propto |W - W_{c,1}|^\phi$ with $\phi = 1.99 \pm 0.03$ and $W_{c,1} < W_c$ (Fig. 4 and Fig. 1). The zero-energy eigenstates are localized at $W_{c,1} < W < W_c$. Firstly, this concludes that zDOS at the localization-delocalization transition point for the CI-DM branch is finite and dynamical exponent z associated with this transition is 3. Note also that, within the self-consistent Born approximation, the exponent ϕ associated with $\rho(0)$ is evaluated as $1/2$ [25], while our numerical observation ($\phi \simeq 2$) clearly deviates from this. Meanwhile, the DOS for different (but small) single-particle energy \mathcal{E} and disorder strength $W > W_{c,1}$ can be well fitted into the same single-parameter scaling function (inset of Fig. 4).

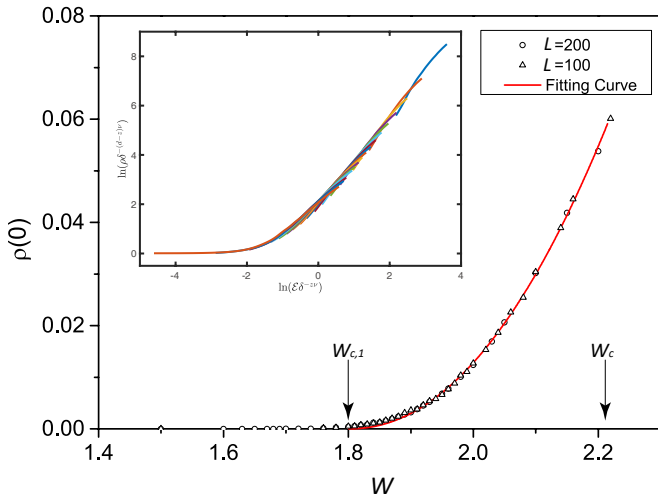


FIG. 4. (color online) zDOS $\rho(0)$ as a function of disorder for $\beta = 0.2$. The data points are fitted by a curve of $\rho(0) \propto \delta^\phi$ with $\phi = 1.99 \pm 0.03$. Inset: Single-parameter scaling of DOS $\rho(\mathcal{E})$ for $\beta = 0.2$, different $W (> W_{c,1})$ and single-particle energy \mathcal{E} with $\rho(\mathcal{E}) > 0.008$. We use $\rho(\mathcal{E}) = \delta^{(d-z)\nu} \Psi(\mathcal{E}\delta^{-z\nu})$ with $\delta \equiv |W - W_{c,1}|/W_{c,1}$, $d = 3$, $z = 1$ and $\nu = 1$ [15].

The critical properties for the CI-DM branch is distinct from that for the WSM-DM branch. This is consistent with the RG flow around the non-trivial fixed point with finite disorder (‘FP1’ in the inset of Fig. 1). Around FP1, the mass term is a relevant scaling variable, so that the critical properties for the CI-DM branch are controlled by saddle-point fixed points at finite $m (< 0)$ and that for the WSM-DM branch is by a saddle-point fixed point at finite $m (> 0)$. Especially, the single-parameter scaling in Fig. 4, $\rho(\mathcal{E}) \sim \delta^{(d-z)\nu} \Psi(\mathcal{E}\delta^{-z\nu})$ [15, 25], suggests that the DOS scaling around the phase boundary between CI with zero zDOS and CI with finite zDOS is controlled by a saddle-point fixed point at finite $m < 0$. From the fitting, we evaluate $\nu \simeq 1$ and $z \simeq 1$ for this (postulated) saddle-point fixed point, which are distinct from those of the conventional 3D unitary class ($\nu_{3d,u} \simeq 1.44$, $z_{3d,u} = 3$). This indicates that there exist two saddle-point fixed points between QMCP at $m = 0$ and the two-dimensional limit with $\beta = 0$. One saddle-point fixed point controls the DOS scaling around the transition between CI phase with zero zDOS and CI phase with finite zDOS. The other fixed point (conventional 3D unitary class) controls critical properties around a localization-delocalization transition between CI with finite zDOS and DM phases (See Appendix C).

VI. CRITICAL EXPONENT FOR CI-WSM BRANCH

To clarify the critical nature of phase transition between CI with zero zDOS and WSM phases, we calculate a localization length along the x_3 -direction at $E = 0$.

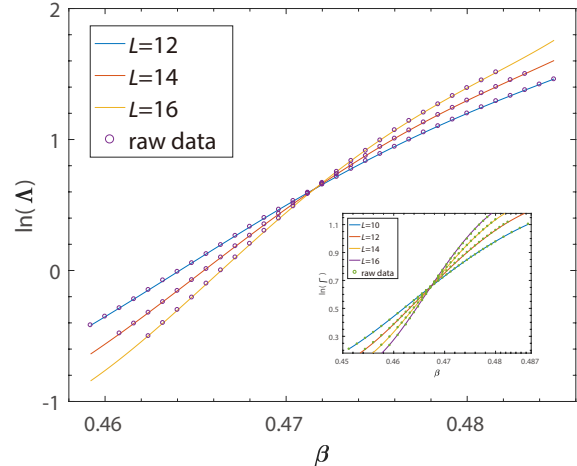


FIG. 5. (color online) $\ln(\Lambda)$ as a function of β at $W = 1$ for the CI-WSM transition with cross-section size $L = 12, 14, 16$. The circle is the raw data and the curves are the fitting result with the expansion orders $(n, m) = (4, 2)$ (see the text). Inset: $\ln(\Gamma)$ as a function of β at $W = 1$ for CI-WSM transition with cross-section size $L = 10, 12, 14, 16$. $\Gamma \equiv \lambda/\sqrt{L}$ and $\Lambda \equiv \lambda/L$ where λ is a localization length along the x_3 direction (see the text).

n	m	GOF	β_c	ν
4	2	0.79	0.4716[0.4715,0.4716]	0.8008[0.7947,0.8068]
5	2	0.95	0.4716[0.4715,0.4716]	0.8002[0.7943,0.8069]
4	3	0.81	0.4716[0.4715,0.4717]	0.8097[0.7964,0.8225]
5	3	0.97	0.4716[0.4715,0.4716]	0.8124[0.7990,0.8261]

TABLE III. Polynomial fitting results with goodness of fit greater than 0.1 are shown with the 95% confidence interval for critical β (β_c) and critical exponent ν .

We fix W and calculate λ by changing β . The calculation is terminated when the precision of Λ reaches 0.2% for $L=12, 14$ and 0.4% for $L=16$. As shown in Fig. 5, curves of Λ for different L intersect almost at the same critical β . We thus use the polynomial fitting without the finite-size correction; $\Lambda = F(\phi_1)$. Table III shows a list of the critical exponent ν and critical mass β_c with different expansion orders; $F(\phi_1) = \sum_{j=0}^n a_j \phi_1^j$ with $\phi_1(\omega) = \sum_{j=1}^m b_j \omega^j$. The fitting with the smallest number of parameters gives $\nu = 0.80$ [0.79, 0.81], which is stable against the increase of the Taylor expansion orders.

According to the RG analyses, the critical property for CI-WSM branch is determined by the fixed point in the clean limit (‘FP0’ in inset of Fig. 1). Around FP0, the mass term is a relevant scaling variable with its scaling dimension $+1$. The critical theory given by Eq. (1) at $m = 0$ has a linear dispersion along the x_1 - x_2 plane, and a quadratic dispersion along the x_3 -direction. This leads to the anisotropic scaling, Eqs. (4) and (5), dictating that a characteristic length scale along x_3 -direction and that along the in-plane direction are scaled with the mass term

differently, $\xi_3 = m^{-\frac{1}{2}}$, $\xi_{\perp} = m^{-1}$. Meanwhile, $\xi_3 = m^{-\frac{1}{2}}$ clearly contradicts with our precise determination of ν .

The discrepancy may be attributed to effect of finite disorders. Though the critical line between CI and WSM phases is controlled by the clean-limit fixed point, any finite small disorder could average out the spatial anisotropy in the scaling property. When a characteristic length scale ξ is defined as a cubic root of a characteristic volume, the scaling exponent of such ξ with respect to m can be around our numerical observation, $\nu_{\text{th}} = \frac{1}{3}(\frac{1}{2} + 1 + 1) = 0.833 \dots$. Nonetheless, we cannot exclude a possibility that the discrepancy simply stems from a crossover phenomenon between FP1 and FP0 either. In fact, the perturbative RG equations given by Eqs. (2) and (3) dictate that the exponent ν at FP1 and FP0 is +1 and +1/2, respectively, while our numerical evaluation places between these two values.

It is also completely legitimate to analyze the obtained numerical data in terms of another scaling theory which stands for the spatially anisotropic scaling dictated by Eqs. (4) and (5). In the new scaling theory, the localization length along the x_3 direction, λ , is normalized by \sqrt{L} instead of L ;

$$\Gamma \equiv \frac{\lambda}{\sqrt{L}}. \quad (32)$$

Namely, L is a linear dimension within the x_1 - x_2 plane and λ is a length scale along the x_3 direction, so that they are scaled by b and $b^{\frac{1}{2}}$ respectively under the anisotropic scaling given by Eqs. (4) and (5); $\lambda' = b^{\frac{1}{2}}\lambda$ and $L' = bL$. Thus, $\Lambda \equiv \lambda/L$ after and before renormalization are related with each other by

$$\Lambda'(m', L') = b^{-\frac{1}{2}}\Lambda(m, L) \quad (33)$$

where $m' = b^{-1}m$ and $L' = bL$. This leads to

$$\Lambda(m, L) = m^{\frac{1}{2}}\Phi(mL). \quad (34)$$

The scaling form dictates that the conventional normalization, $\Lambda \equiv \lambda/L$, does not give a function only of mL . Instead, the new normalization, $\Gamma \equiv \lambda/\sqrt{L}$, does give a function only of mL ;

$$\begin{aligned} \Gamma(m, L) &= \Lambda(m, L)L^{\frac{1}{2}} \\ &= (mL)^{\frac{1}{2}}\Phi(mL) = f(mL). \end{aligned} \quad (35)$$

Our fitting based on Eqs. (32) and (35) shows a scaling invariant point at $\beta = \beta'_c < \beta_c$. Meanwhile, an exponent ν' defined as $\Gamma \equiv f(m^{\nu'}L)$ is evaluated to be around 0.75 at $W = 1$ rather than the expected value (1).

VII. CONCLUSION AND OUTLOOK

In this paper, we reveal a novel disorder-driven quantum multicriticality in disordered Weyl semimetal, by clarifying a rich variety of universal scalings of low-energy

density of states (DOS), diffusion constants, and conductivities around the quantum multicritical point (QMCP) that is encompassed by three quantum phases; CI, WSM and DM phases. We show that, around a quantum critical line between CI and WSM phases, conductivities as well as diffusion constants in one spatial direction obey different universal scaling with different exponents from those in the other spatial directions. As for a phase boundary between CI and DM phases, we numerically demonstrated that a mobility edge and band edge are distinct in a phase diagram. We further show that the mobility edge belongs to the conventional 3D unitary class, while the DOS scaling around the band edge is controlled by another fixed point with different critical and dynamical exponents. We also confirmed numerically that the phase transition between CI and WSM is direct, and an associated critical exponent and scaling behaviour are rather consistent with the RG analyses than inconsistent.

The usage of the disordered magnetic dipole model and its RG analyses are not limited to the QMCP encompassed by CI, WSM and DM phases, though our simulation focused on this particular critical point. Being derived by the $\mathbf{k} \cdot \mathbf{p}$ expansion around high symmetric points, the dipole model does not carry any information of global \mathbf{k} -space topology in its gapped phase side. Thus, scaling properties revealed in this paper can be equally applicable to the other QMCP that is encompassed by ordinary three-dimensional band insulator, WSM and, DM phases [24–27].

Layered organic conductors may offer an experimental platform for exploring conductivity scalings discussed in this paper [46–48]. Being soft, organic materials under an uniaxial pressure acquire substantial changes in hopping integrals among molecular orbitals, which sometimes result in a formation of a pair of two-dimensional gapless Dirac fermions in their electrotonic band structures [46, 47]. Thereby, the in-plane uniaxial pressure continuously changes the location of the gapless points in the \mathbf{k} -space, and it is predicted that the pair of the two Dirac points annihilate with each other above a certain critical pressure [46, 47, 49, 50]. In such layered conductors, the out-of-plane uniaxial pressure can also enhance interlayer hopping strengths, which may lead to a formation and pair annihilation of three-dimensional gapless Dirac or Weyl points with or without the relativistic spin-orbit interaction [1, 51]. Further detailed studies in conjunction with the ab-initio band calculation along this direction are awaited.

Appendix A: Tight-Binding Cubic-Lattice Model for Weyl Semimetal

We use the same two-orbital tight-binding model on a cubic lattice as studied previously [24–27, 31, 32]. The model consists of an s orbital and a $p = p_x + ip_y$ orbital

on each cubic lattice site (\mathbf{x});

$$\begin{aligned} \mathcal{H} = & \sum_{\mathbf{x}} \left\{ (\epsilon_s + v_s(\mathbf{x})) c_{\mathbf{x},s}^\dagger c_{\mathbf{x},s} + (\epsilon_p + v_p(\mathbf{x})) c_{\mathbf{x},p}^\dagger c_{\mathbf{x},p} \right\} \\ & + \sum_{\mathbf{x}} \left\{ - \sum_{\mu=1,2} (t_s c_{\mathbf{x}+\mathbf{e}_\mu,s}^\dagger c_{\mathbf{x},s} - t_p c_{\mathbf{x}+\mathbf{e}_\mu,p}^\dagger c_{\mathbf{x},p}) \right. \\ & + t_{sp} (c_{\mathbf{x}+\mathbf{e}_1,p}^\dagger - c_{\mathbf{x}-\mathbf{e}_1,p}^\dagger - i c_{\mathbf{x}+\mathbf{e}_2,p}^\dagger + i c_{\mathbf{x}-\mathbf{e}_2,p}^\dagger) c_{\mathbf{x},s} \\ & \left. - t'_s c_{\mathbf{x}+\mathbf{e}_3,s}^\dagger c_{\mathbf{x},s} - t'_p c_{\mathbf{x}+\mathbf{e}_3,p}^\dagger c_{\mathbf{x},p} + \text{H.c.} \right\}. \quad (\text{A1}) \end{aligned}$$

ϵ_s , ϵ_p and $v_s(\mathbf{x})$, $v_p(\mathbf{x})$, are atomic energies for the s , p orbital and on-site disorder potential of the s , p orbital, respectively. The disorder potentials are uniformly distributed within $[-W/2, W/2]$ with identical probability distribution. t_s , t_p , and t_{sp} are intralayer transfer integrals between s orbitals of nearest neighboring two sites, that between p orbitals, and that between s and p orbitals, respectively, while t'_s and t'_p are interlayer transfer integrals. \mathbf{e}_μ ($\mu = 1, 2$) are primitive translational vectors within a square-lattice plane. \mathbf{e}_3 is a primitive translational vector connecting neighboring square-lattice layers. Without the interlayer transfers, the electron model in the clean limit at half electron filling (one electron filling per cubic lattice site) is in either one of the two (layered) Chern band insulator phases ($0 < \epsilon_s - \epsilon_p < 4(t_s + t_p)$, $-4(t_s + t_p) < \epsilon_s - \epsilon_p < 0$) or in the ordinary insulator phase ($4(t_s + t_p) < |\epsilon_s - \epsilon_p|$). In this paper, we take $\epsilon_s - \epsilon_p = -2(t_s + t_p)$, $t_s = t_p > 0$, and $t_{sp} = 4t_s/3$. A larger interlayer coupling induces a phase transition from the layered Chern band insulator phase to Weyl semimetal phase. In this paper, we take $t'_s = -t'_p > 0$. For $\beta \equiv (t'_s - t'_p)/[2(t_s + t_p)]$ greater than $1/2$, a Fourier-transformed tight-binding Hamiltonian has three pairs of Weyl nodes at $\mathbf{k} = (\pi, \pi, \pm k_0)$, $(0, \pi, \pi \pm k_0)$ and $(\pi, 0, \pi \pm k_0)$ with $\cos k_0 \equiv \frac{1}{2\beta}$. In a clean-limit phase diagram subtended by β , a quantum critical point ($\beta = 1/2$) intervenes the (Chern) band insulator phase ($\beta < 1/2$) and a Weyl semimetal phase with three pairs of Weyl nodes ($\beta > 1/2$).

Appendix B: Renormalization Group Analyses for Low-Energy Effective Electron Hamiltonian with Disorders

At the quantum critical point, three pairs of Weyl nodes annihilate at the high symmetric \mathbf{k} points; $\mathbf{k} = (\pi, \pi, 0)$, $(\pi, 0, \pi)$ and $(0, \pi, \pi)$, respectively. Each pair annihilation is described by the following two by two effective Hamiltonian, which is obtained from the $\mathbf{k} \cdot \mathbf{p}$ expansion around these high symmetric \mathbf{k} points;

$$\mathbf{H}_{\text{eff}}(\mathbf{p}) = v(p_1 \boldsymbol{\sigma}_1 + p_2 \boldsymbol{\sigma}_2) + (b_2 p_3^2 - m) \boldsymbol{\sigma}_3. \quad (\text{B1})$$

Here $\mathbf{p} \equiv (p_1, p_2, p_3)$ denotes a crystal momentum measured from the symmetric \mathbf{k} points. Velocities along the x_1 and x_2 directions are same due to the C_4 rotational symmetry. For $m < 0$, the effective Hamiltonian

is gapped for the half-filling case (Chern band insulator phase), while, for $m > 0$, the Hamiltonian has a pair of Weyl nodes at $(p_1, p_2, p_3) = (0, 0, \pm \sqrt{m/b_2})$.

Effect of disorders on the quantum critical point can be studied by the following replicated effective action [37, 45],

$$\begin{aligned} Z &= \int d\psi_\alpha^\dagger \psi_\alpha e^{-S}, \quad S = S_0 + S_1, \\ S_0 &\equiv \int d\tau \int d^2 \mathbf{x}_\perp dx_3 \psi_\alpha^\dagger(\mathbf{x}, \tau) \left\{ a \partial_\tau - iv(\partial_1 \boldsymbol{\sigma}_1 + \partial_2 \boldsymbol{\sigma}_2) \right. \\ &\quad \left. + ((-i)^2 b_2 \partial_3^2 - m) \boldsymbol{\sigma}_3 \right\} \psi_\alpha(\mathbf{x}, \tau) \quad (\text{B2}) \\ S_1 &\equiv -\frac{\Delta_0}{2} \int d\tau \int d\tau' \int d^3 \mathbf{x} (\psi_\alpha^\dagger \psi_\alpha)_{\mathbf{x},\tau} (\psi_\beta^\dagger \psi_\beta)_{\mathbf{x},\tau'} \\ &\quad - \frac{\Delta_3}{2} \int d\tau \int d\tau' \int d^3 \mathbf{x} (\psi_\alpha^\dagger \boldsymbol{\sigma}_3 \psi_\alpha)_{\mathbf{x},\tau} (\psi_\beta^\dagger \boldsymbol{\sigma}_3 \psi_\beta)_{\mathbf{x},\tau'} \\ &\quad - \frac{\Delta_\perp}{2} \sum_{\mu=1,2} \int d\tau \int d\tau' \int d^3 \mathbf{x} (\psi_\alpha^\dagger \boldsymbol{\sigma}_\mu \psi_\alpha)_{\mathbf{x},\tau} (\psi_\beta^\dagger \boldsymbol{\sigma}_\mu \psi_\beta)_{\mathbf{x},\tau'} \quad (\text{B3}) \end{aligned}$$

where a coefficient in front of ∂_τ in S_0 is for a bookkeeping purpose; $a = 1$. Here we have considered only short-ranged correlated on-site disorders in the low-energy effective Hamiltonian,

$$\begin{aligned} \mathcal{H}_{\text{eff}} &= \int d^3 \mathbf{x} \psi^\dagger(\mathbf{x}) \left\{ -iv(\partial_1 \boldsymbol{\sigma}_1 + \partial_2 \boldsymbol{\sigma}_2) + \right. \\ &\quad \left. ((-i)^2 b_2 \partial_3^2 - m) \boldsymbol{\sigma}_3 + \sum_{\mu=0,1,2,3} V_\mu(\mathbf{x}) \boldsymbol{\sigma}_\mu \right\} \psi(\mathbf{x}), \quad (\text{B4}) \end{aligned}$$

with $\langle V_\mu(\mathbf{x}) V_\nu(\mathbf{x}') \rangle_{\text{imp}} = \Delta_\mu \delta_{\mu\nu} \delta^3(\mathbf{x} - \mathbf{x}')$, and $\Delta_1 = \Delta_2 \equiv \Delta_\perp$. The summation over the replica indices α and β are omitted ($\alpha, \beta = 1, \dots, N$). In the perturbative derivation of renormalization group equations, we only keep those Feynman diagram contributions which survive in the limit of $N \rightarrow 0$. Following Roy et. al [31], we employ a momentum-shell renormalization method, to decompose the fermion field ψ_α into a slow mode ($\psi_{\alpha,<}$) and a fast mode ($\psi_{\alpha,>}$) in the momentum space,

$$\begin{aligned} \psi_\alpha(\mathbf{x}, \tau) &= \psi_{\alpha,<}(\mathbf{x}, \tau) + \psi_{\alpha,>}(\mathbf{x}, \tau) \\ &= \frac{1}{\sqrt{\beta V}} \sum_{i\mathcal{E}_n, \mathbf{p}}^{p_\perp < \Lambda e^{-d\tau}} e^{i\mathbf{p}\mathbf{x} - i\mathcal{E}_n \tau} \psi_\alpha(\mathbf{p}, \mathcal{E}_n) \\ &\quad + \frac{1}{\sqrt{\beta V}} \sum_{i\mathcal{E}_n, \mathbf{p}}^{\Lambda e^{-d\tau} < p_\perp < \Lambda} e^{i\mathbf{p}\mathbf{x} - i\mathcal{E}_n \tau} \psi_\alpha(\mathbf{p}, \mathcal{E}_n). \end{aligned}$$

with $p_\perp \equiv \{p_1^2 + p_2^2\}^{\frac{1}{2}}$. The integration of the fast mode ($>$) in the partition function leads to a renormalization

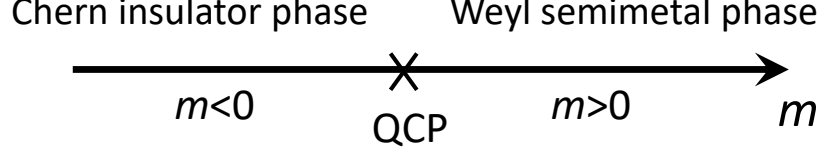


FIG. 6. Schematic phase diagram for a quantum critical point intervening layered (Chern) band insulator phase ($m < 0$) and Weyl semimetal phase ($m > 0$). $m < 0$ corresponds to $\beta < \frac{1}{2}$ and $m > 0$ to $\beta > \frac{1}{2}$ in the LCI model in this paper.

of effective action for the slow mode ($<$),

$$\begin{aligned}
 Z &= \int d\psi_{\alpha,<}^\dagger d\psi_{\alpha,<} e^{-S_{0,<}} e^{-S_{1,<}} \int d\psi_{\alpha,>}^\dagger d\psi_{\alpha,>} e^{-S_{0,>}} e^{-S_{1,>}} \\
 &\equiv Z_{0,>} \int d\psi_{\alpha,<}^\dagger d\psi_{\alpha,<} e^{-S_{0,<}} e^{-S_{1,<}} \langle e^{-S_{1,>}} \rangle_{0,>} \\
 &= Z_{0,>} \int d\psi_{\alpha,<}^\dagger d\psi_{\alpha,<} e^{-S_{0,<}} e^{-S_{1,<}} \\
 &\quad e^{-\langle S_{1,>} \rangle_{0,>} + \frac{1}{2} (\langle S_{1,>}^2 \rangle_{0,>} - \langle S_{1,>} \rangle_{0,>}^2) + \dots}
 \end{aligned} \tag{B5}$$

where

$$\begin{aligned}
 \langle \dots \rangle_{0,>} &\equiv \frac{1}{Z_{0,>}} \int d\psi_{\alpha,>}^\dagger d\psi_{\alpha,>} e^{-S_{0,>}} \dots, \\
 Z_{0,>} &\equiv \int d\psi_{\alpha,>}^\dagger d\psi_{\alpha,>} e^{-S_{0,>}}
 \end{aligned}$$

and

$$\begin{aligned}
 S_{1,>} &= -\frac{\Delta_0}{2} \int d\tau \int d\tau' \int d^3\mathbf{x} \left\{ 2(\psi_{\alpha,>}^\dagger \psi_{\alpha,>})_{\mathbf{x},\tau} (\psi_{\beta,<}^\dagger \psi_{\beta,<})_{\mathbf{x},\tau'} + 2(\psi_{\alpha,<}^\dagger \psi_{\alpha,>})_{\mathbf{x},\tau} (\psi_{\beta,>}^\dagger \psi_{\beta,<})_{\mathbf{x},\tau'} \right. \\
 &\quad \left. + (\psi_{\alpha,>}^\dagger \psi_{\alpha,<})_{\mathbf{x},\tau} (\psi_{\beta,>}^\dagger \psi_{\beta,<})_{\mathbf{x},\tau'} + (\psi_{\alpha,<}^\dagger \psi_{\alpha,>})_{\mathbf{x},\tau} (\psi_{\beta,<}^\dagger \psi_{\beta,>})_{\mathbf{x},\tau'} \right\} - \frac{\Delta_3}{2} \int \dots - \frac{\Delta_\perp}{2} \sum_{\mu=1,2} \int \dots
 \end{aligned} \tag{B6}$$

$$S_{0,>(<)} = \sum_{i\mathcal{E}_n} \sum_{p_3} \sum_{p_\perp}' \psi_{\alpha}'^\dagger(\mathbf{p}, \mathcal{E}_n) \left\{ -i\mathcal{E}_n a \boldsymbol{\sigma}_0 + v(p_1 \boldsymbol{\sigma}_1 + p_2 \boldsymbol{\sigma}_2) + (b_2 p_3^2 - m) \boldsymbol{\sigma}_3 \right\} \psi_{\alpha}(\mathbf{p}, \mathcal{E}_n). \tag{B7}$$

The integral region over \mathbf{p} in $S_{0,>(<)}$ is restricted within the fast mode (slow mode). $S_{1,<}$ comprises only of the slow modes. We keep only those terms in Eq. (B5) which survive in the zero-replica limit ($N \rightarrow 0$) [10, 12, 20, 21, 31];

$$\begin{aligned}
 \langle S_{1,>} \rangle_{0,>} &= -(\Delta_0 + 2\Delta_\perp + \Delta_3) \sum_{i\mathcal{E}_n} \sum_{\mathbf{p}}' h_0 i\mathcal{E}_n \psi_{\alpha,<}^\dagger(\mathbf{p}, i\mathcal{E}_n) \boldsymbol{\sigma}_0 \psi_{\alpha,<}(\mathbf{p}, i\mathcal{E}_n) \\
 &\quad - (\Delta_0 - 2\Delta_\perp + \Delta_3) \sum_{i\mathcal{E}_n} \sum_{\mathbf{p}}' h_1 \psi_{\alpha,<}^\dagger(\mathbf{p}, i\mathcal{E}_n) \boldsymbol{\sigma}_3 \psi_{\alpha,<}(\mathbf{p}, i\mathcal{E}_n)
 \end{aligned} \tag{B8}$$

with

$$h_0 = \frac{1}{V} \sum_{p_3} \sum_{\Lambda e^{-dl} < p_\perp < \Lambda} \frac{1}{\mathcal{E}_n^2 + v^2 p_\perp^2 + (b_2 p_3^2 - m)^2} = \frac{\Lambda^2 dl}{4\pi^2} \int_{-\infty}^{+\infty} \frac{dp_3}{(v\Lambda)^2 + (b_2 p_3^2 - m)^2} \equiv H_0 dl \tag{B9}$$

$$h_1 = \frac{1}{V} \sum_{p_3} \sum_{\Lambda e^{-dl} < p_\perp < \Lambda} \frac{b_2 p_3^2 - m}{\mathcal{E}_n^2 + v^2 p_\perp^2 + (b_2 p_3^2 - m)^2} = \frac{\Lambda^2 dl}{4\pi^2} \int_{-\infty}^{+\infty} dp_3 \frac{b_2 p_3^2 - m}{(v\Lambda)^2 + (b_2 p_3^2 - m)^2} \equiv H_1 dl \tag{B10}$$

and

$$\begin{aligned} & \frac{1}{2} (\langle S_{1,>}^2 \rangle_{0,>} - \langle S_{1,>} \rangle_{0,>}^2) \\ &= \frac{1}{V} \sum_{\mu=0,1,2,3} \sum_{i\mathcal{E}} \sum_{i\mathcal{E}'} \sum_{\mathbf{p},\mathbf{p}',\mathbf{q}}' F_{\mu} (\psi_{\alpha,<}^{\dagger}(\mathbf{p} + \mathbf{q}, i\mathcal{E}) \sigma_{\mu} \psi_{\alpha,<}(\mathbf{p}, i\mathcal{E})) (\psi_{\alpha,<}^{\dagger}(\mathbf{p}' - \mathbf{q}, i\mathcal{E}') \sigma_{\mu} \psi_{\alpha,<}(\mathbf{p}', i\mathcal{E}')) \end{aligned} \quad (\text{B11})$$

with

$$F_0 = (h_2 + h_3)\Delta_0^2 + (h_2 + 3h_3)\Delta_0\Delta_3 + 2(h_2 + h_3)\Delta_0\Delta_{\perp} + 2h_2\Delta_3\Delta_{\perp} \quad (\text{B12})$$

$$F_3 = h_3\Delta_0^2 + (-h_2 + 2h_3)\Delta_3^2 + 2h_3\Delta_{\perp}^2 + (-h_2 + h_3)\Delta_0\Delta_3 + 2h_2\Delta_0\Delta_{\perp} + 2(h_2 - h_3)\Delta_3\Delta_{\perp} \quad (\text{B13})$$

$$F_1 = F_2 = h_2\Delta_0\Delta_3 - h_3\Delta_0\Delta_{\perp} + 3h_3\Delta_3\Delta_{\perp} \quad (\text{B14})$$

and

$$\begin{aligned} h_2 &= \frac{\Lambda^2 dl}{4\pi^2} \int_{-\infty}^{+\infty} \frac{(v\Lambda)^2 dp_3}{[(v\Lambda)^2 + (b_2 p_3^2 - m)^2]^2} \equiv H_2 dl, \\ h_3 &= \frac{\Lambda^2 dl}{4\pi^2} \int_{-\infty}^{+\infty} \frac{(b_2 p_3^2 - m)^2 dp_3}{[(v\Lambda)^2 + (b_2 p_3^2 - m)^2]^2} \equiv H_3 dl. \end{aligned} \quad (\text{B15})$$

To evaluate h_0, h_1, h_2, h_3 , we have set the frequencies and momenta for the slow modes (external lines) to zero [10, 12, 20, 21, 31]. After the integration over the fast modes, we scale spatial coordinate, time and field operators as

$$\psi_{\alpha} = Z_{\psi}^{-\frac{1}{2}} \psi'_{\alpha} \equiv e^{-\frac{g dl}{2}} \psi'_{\alpha}, \quad (\text{B16})$$

$$\tau = e^{z dl} \tau', \quad (\text{B17})$$

$$\mathbf{x}_{\perp} = e^{dl} \mathbf{x}'_{\perp}, \quad (\text{B18})$$

$$x_3 = e^{\frac{dl}{2}} x'_3. \quad (\text{B19})$$

This leads to one-loop renormalization for a, v, b_2, Δ_0 ,

Δ_3 and Δ_{\perp} ,

$$a' = a + (2 + \frac{1}{2} - g)a dl + (\Delta_0 + 2\Delta_{\perp} + \Delta_3)h_0, \quad (\text{B20})$$

$$v' = v + (1 + \frac{1}{2} + z - g)v dl, \quad (\text{B21})$$

$$b'_2 = b_2 + (1 + \frac{1}{2} + z - g)b_2 dl, \quad (\text{B22})$$

$$m' = m + (2 + \frac{1}{2} + z - g)m dl + (\Delta_0 - 2\Delta_{\perp} + \Delta_3)h_1, \quad (\text{B23})$$

$$\Delta'_0 = \Delta_0 + (2 + \frac{1}{2} + 2z - 2g)\Delta_0 dl + F_0, \quad (\text{B24})$$

$$\Delta'_3 = \Delta_3 + (2 + \frac{1}{2} + 2z - 2g)\Delta_3 dl + F_3, \quad (\text{B25})$$

$$\Delta'_{\perp} = \Delta_{\perp} + (2 + \frac{1}{2} + 2z - 2g)\Delta_{\perp} dl + F_{\perp}. \quad (\text{B26})$$

We choose a scaling of the field operator g and dynamical exponent z in a way that a gapless part of the effective action (a, v and b_2 in Eq. (B2)) is invariant under the renormalization [10, 12, 20, 21, 31];

$$g = (2 + \frac{1}{2}) + (\Delta_0 + 2\Delta_{\perp} + \Delta_3)H_0, \quad (\text{B27})$$

$$z = 1 + (\Delta_0 + 2\Delta_{\perp} + \Delta_3)H_0. \quad (\text{B28})$$

Using this, we obtain from Eqs. (B23)-(B26) one-loop renormalization group equations for mass (m) and three kinds of disorder strength;

$$\frac{dm}{dl} = m + (\Delta_0 - 2\Delta_{\perp} + \Delta_3)H_1, \quad (\text{B29})$$

$$\frac{d\Delta_0}{dl} = -\frac{1}{2}\Delta_0 + (H_2 + H_3)(\Delta_0 + 2\Delta_{\perp} + \Delta_3)\Delta_0 + 2H_3\Delta_0\Delta_3 + 2H_2\Delta_3\Delta_{\perp}, \quad (\text{B30})$$

$$\frac{d\Delta_{\perp}}{dl} = -\frac{1}{2}\Delta_{\perp} + H_2\Delta_0\Delta_3 - H_3\Delta_0\Delta_{\perp} + 3H_3\Delta_3\Delta_{\perp}, \quad (\text{B31})$$

$$\frac{d\Delta_3}{dl} = -\frac{1}{2}\Delta_3 + (-H_2 + H_3)(\Delta_0 - 2\Delta_{\perp} + \Delta_3)\Delta_3 + H_3(\Delta_0^2 + 2\Delta_{\perp}^2 + \Delta_3^2) + 2H_2\Delta_0\Delta_{\perp}, \quad (\text{B32})$$

To make the RG analysis to be a controlled analysis, Roy et.al. proposed to replace $b_2(-i)^2\partial_3^2$ in Eqs. (B1) and (B4) by $b_n(-i)^n\partial_3^n$ [31]. This leads to replacements of $b_2p_3^2$ in Eqs. (B9), (B10), and (B15) by $b_np_3^n$ and $\frac{1}{2}$ in Eqs. (B19)-(B27) and (B30)-(B32) by $\frac{1}{n}$. Thereby, disorder strength of any non-trivial fixed point becomes on the order of $1/n$ in a large n limit, which always justifies the above perturbative derivation of the RG equation in the leading order of $1/n$. All the scaling analyses based on the RG equation around such fixed points become controlled in the large n limit. For general even integer n , we have

$$H_0 = \frac{\Lambda^2}{4\pi^2} \int_{-\infty}^{+\infty} dX \frac{1}{(v\Lambda)^2 + (b_n X^n - m)^2} = \frac{\Lambda^2 R^{\frac{1}{n}-2}}{4\pi^2 b_n^{\frac{1}{n}}} \frac{2\pi \sin[(n-1)\phi_n]}{n \sin[n\phi_n]} \frac{1}{\sin[\frac{\pi}{n}]}, \quad (\text{B33})$$

$$H_1 = \frac{\Lambda^2}{4\pi^2} \int_{-\infty}^{+\infty} dX \frac{b_n X^n - m}{(v\Lambda)^2 + (b_n X^n - m)^2} = \frac{\Lambda^2 R^{\frac{1}{n}-1}}{4\pi^2 b_n^{\frac{1}{n}}} \frac{2\pi \sin[\phi_n] + \cos[n\phi_n] \sin[(n-1)\phi_n]}{n \sin[n\phi_n]} \frac{1}{\sin[\frac{\pi}{n}]}, \quad (\text{B34})$$

$$H_2 = \frac{\Lambda^2}{4\pi^2} \int_{-\infty}^{+\infty} dX \frac{(v\Lambda)^2}{[(v\Lambda)^2 + (b_n X^n - m)^2]^2} = \frac{\Lambda^2 R^{\frac{1}{n}-2}}{4\pi^2 b_n^{\frac{1}{n}}} \frac{\pi}{n \sin[\frac{\pi}{n}]} \left(\frac{\sin[(n-1)\phi_n]}{\sin[n\phi_n]} - \frac{n-1}{n} \cos[(2n-1)\phi_n] \right), \quad (\text{B35})$$

$$H_3 = \frac{\Lambda^2}{4\pi^2} \int_{-\infty}^{+\infty} dX \frac{(b_n X^n - m)^2}{[(v\Lambda)^2 + (b_n X^n - m)^2]^2} = \frac{\Lambda^2 R^{\frac{1}{n}-2}}{4\pi^2 b_n^{\frac{1}{n}}} \frac{\pi}{n \sin[\frac{\pi}{n}]} \left(\frac{\sin[(n-1)\phi_n]}{\sin[n\phi_n]} + \frac{n-1}{n} \cos[(2n-1)\phi_n] \right). \quad (\text{B36})$$

with $H_2 + H_3 \equiv H_0$. $n\phi_n$ measures an angle subtended by the mass m and cutoff energy $v\Lambda$ (see Fig. 7).

1. large- n limit

In the large n limit, the leading order contribution of H_0 , H_1 , H_2 , H_3 are as follows,

$$H_0 = \frac{\Lambda^2 R^{\frac{1}{n}-2}}{4\pi^2 b_n^{\frac{1}{n}}} \left\{ 2 + \mathcal{O}(n^{-1}) \right\}, H_1 = \frac{\Lambda^2 R^{\frac{1}{n}-1}}{4\pi^2 b_n^{\frac{1}{n}}} \left\{ -\frac{2m}{R} + \mathcal{O}(n^{-1}) \right\},$$

$$H_2 = \frac{\Lambda^2 R^{\frac{1}{n}-2}}{4\pi^2 b_n^{\frac{1}{n}}} \left\{ \frac{2(v\Lambda)^2}{R^2} + \mathcal{O}(n^{-1}) \right\}, H_3 = \frac{\Lambda^2 R^{\frac{1}{n}-2}}{4\pi^2 b_n^{\frac{1}{n}}} \left\{ \frac{2m^2}{R^2} + \mathcal{O}(n^{-1}) \right\}.$$

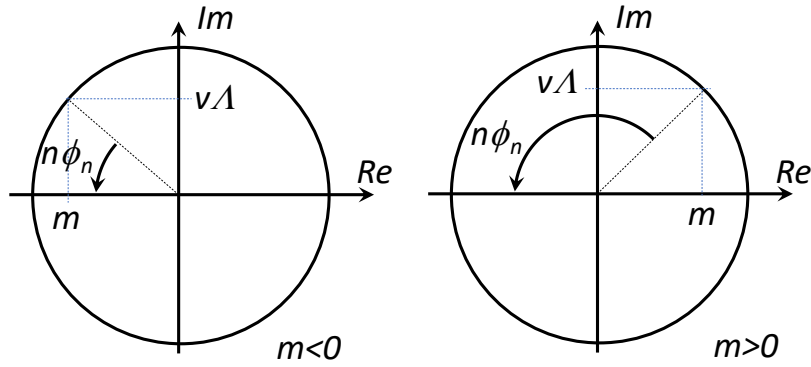


FIG. 7. $n\phi_n$ is an angle subtended by the mass m and cutoff energy $v\Lambda$ with $\cos[n\phi_n] = -\frac{m}{R}$ and $R = \{m^2 + (v\Lambda)^2\}^{\frac{1}{2}}$. (Left) $m < 0$, (Right) $m > 0$.

The RG equations in the large n limit take form of

$$z = 1 + 2(\bar{\Delta}_0 + 2\bar{\Delta}_\perp + \bar{\Delta}_3), \quad (\text{B37})$$

$$\frac{dm}{dl} = m - 2m(\bar{\Delta}_0 - 2\bar{\Delta}_\perp + \bar{\Delta}_3) \left(\frac{v\Lambda}{R}\right)^{2-\frac{1}{n}}, \quad (\text{B38})$$

$$\frac{d\bar{\Delta}_0}{dl} = -\frac{1}{n}\bar{\Delta}_0 + 2(\bar{\Delta}_0 + 2\bar{\Delta}_\perp + \bar{\Delta}_3)\bar{\Delta}_0 \left(\frac{v\Lambda}{R}\right)^{2-\frac{1}{n}} + 4\bar{\Delta}_0\bar{\Delta}_3 \left(\frac{m}{R}\right)^2 \left(\frac{v\Lambda}{R}\right)^{2-\frac{1}{n}} + 4\bar{\Delta}_3\bar{\Delta}_\perp \left(\frac{v\Lambda}{R}\right)^{4-\frac{1}{n}}, \quad (\text{B39})$$

$$\frac{d\bar{\Delta}_\perp}{dl} = -\frac{1}{n}\bar{\Delta}_\perp + 2\bar{\Delta}_0\bar{\Delta}_3 \left(\frac{v\Lambda}{R}\right)^{4-\frac{1}{n}} - 2\bar{\Delta}_0\bar{\Delta}_\perp \left(\frac{m}{R}\right)^2 \left(\frac{v\Lambda}{R}\right)^{2-\frac{1}{n}} + 6\bar{\Delta}_3\bar{\Delta}_\perp \left(\frac{m}{R}\right)^2 \left(\frac{v\Lambda}{R}\right)^{2-\frac{1}{n}}, \quad (\text{B40})$$

$$\begin{aligned} \frac{d\bar{\Delta}_3}{dl} = & -\frac{1}{n}\bar{\Delta}_3 + 2(\bar{\Delta}_0 - 2\bar{\Delta}_\perp + \bar{\Delta}_3)\bar{\Delta}_3 \frac{m^2 - (v\Lambda)^2}{R^2} \left(\frac{v\Lambda}{R}\right)^{2-\frac{1}{n}} \\ & + 2(\bar{\Delta}_0^2 + 2\bar{\Delta}_\perp^2 + \bar{\Delta}_3^2) \left(\frac{m}{R}\right)^2 \left(\frac{v\Lambda}{R}\right)^{2-\frac{1}{n}} + 4\bar{\Delta}_0\bar{\Delta}_\perp \left(\frac{v\Lambda}{R}\right)^{4-\frac{1}{n}}, \end{aligned} \quad (\text{B41})$$

with $R^2 \equiv m^2 + (v\Lambda)^2$ and

$$\bar{\Delta}_\mu \equiv \Delta_\mu \cdot \frac{(v\Lambda)^{\frac{1}{n}}}{4\pi^2 v^2 b_n^{\frac{1}{n}}}. \quad (\text{B42})$$

In the leading order expansion in large n , we can replace $(v\Lambda/R)^{2-\frac{1}{n}}$ and $(v\Lambda/R)^{4-\frac{1}{n}}$ in the right hand sides of Eqs. (B38)-(B41) by $(v\Lambda/R)^2$ and $(v\Lambda/R)^4$, respectively. Note also that the RG equations differ from RG equations obtained by Roy et. al. [31] in several aspects. First of all, (i) $-2m$ in Eq. (B38) is $+m$ in the RG equations by Roy et. al. [31], (ii) $2(\bar{\Delta}_0 + 2\bar{\Delta}_\perp + \bar{\Delta}_3)$ in Eq. (B37) is $\bar{\Delta}_0 + 2\bar{\Delta}_\perp + \bar{\Delta}_3$ in Roy et. al. [31] These differences change the scaling exponent of m and a dynamical exponent z , respectively as well as the DOS, diffusion constant and conductivities scalings around the quantum multicritical point (see the next section). Besides, we keep m/R to be finite, instead of setting m/R and Λ/R to be zero and unit, respectively [31].

The set of RG equations above have only one non-trivial fixed point and a trivial fixed point;

$$\text{FP0} : (z, m, \bar{\Delta}_0, \bar{\Delta}_\perp, \bar{\Delta}_3) = (1, 0, 0, 0, 0), \quad (\text{B43})$$

$$\text{FP1} : (z, m, \bar{\Delta}_0, \bar{\Delta}_\perp, \bar{\Delta}_3) = \left(1 + \frac{1}{n}, 0, \frac{1}{2n}, 0, 0\right). \quad (\text{B44})$$

These two fixed points are on a plane of $\bar{\Delta}_3 = \bar{\Delta}_\perp = 0$. Besides, any points in the plane of $\Delta_3 = \Delta_\perp = 0$ flows within the same plane. The former fixed point FP0 is a saddle point of the RG flow around which the RG equations are linearized as

$$\frac{dm}{dl} = m, \quad \frac{d\Delta_0}{dl} = -\frac{1}{n}\Delta_0. \quad (\text{B45})$$

The latter fixed point FP1 is an unstable point of the RG flow, around which linearized equations take forms of

$$\frac{dm}{dl} = \left(1 - \frac{1}{n}\right)m, \quad \frac{d\Delta_0}{dl} = \frac{1}{n}(\Delta_0 - \frac{1}{2n}). \quad (\text{B46})$$

2. in the case of $n = 2$

For complementary information, we also analyze the RG equations in the case of $n = 2$, where

$$\begin{aligned} H_0 &= \frac{\Lambda^2 R^{\frac{1}{2}-2} \pi}{4\pi^2 b_2^{\frac{1}{2}}} \frac{1}{2 \cos[\phi_2]}, \quad H_1 = \frac{\Lambda^2 R^{\frac{1}{2}-1}}{4\pi^2 b_2^{\frac{1}{2}}} \pi \cos[\phi_2], \\ H_2 &= \frac{\Lambda^2 R^{\frac{1}{2}-2} \pi}{4\pi^2 b_2^{\frac{1}{2}}} \frac{1}{4} \left\{ \frac{1}{\cos[\phi_2]} - \cos[3\phi_2] \right\}, \\ H_3 &= \frac{\Lambda^2 R^{\frac{1}{2}-2} \pi}{4\pi^2 b_2^{\frac{1}{2}}} \frac{1}{4} \left\{ \frac{1}{\cos[\phi_2]} + \cos[3\phi_2] \right\}. \end{aligned}$$

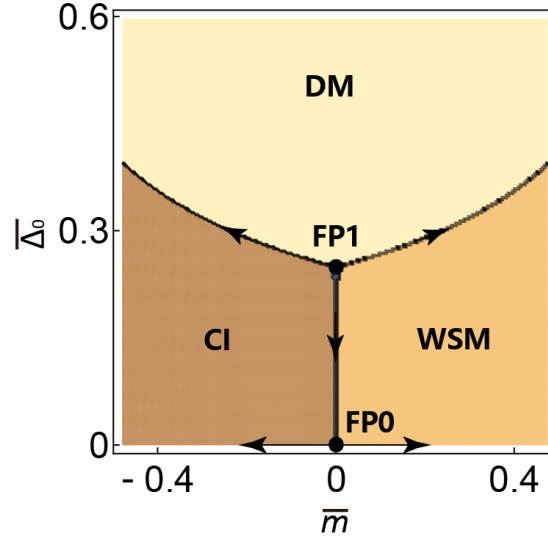


FIG. 8. (color online) Phase diagram in $\bar{\Delta}_0$ - \bar{m} plane determined by the RG equations in the large n limit.

A set of the RG equations is simplified as follows,

$$z = 1 + 2(\bar{\Delta}_0 + 2\bar{\Delta}_\perp + \bar{\Delta}_3) \left(\frac{v\Lambda}{R}\right)^{2-\frac{1}{2}} x, \quad (\text{B47})$$

$$\frac{dm}{dl} = m + 4R(\bar{\Delta}_0 - 2\bar{\Delta}_\perp + \bar{\Delta}_3) \left(\frac{v\Lambda}{R}\right)^{2-\frac{1}{2}} y, \quad (\text{B48})$$

$$\frac{d\bar{\Delta}_0}{dl} = -\frac{1}{2}\bar{\Delta}_0 + 2(\bar{\Delta}_0 + 2\bar{\Delta}_\perp + \bar{\Delta}_3)\bar{\Delta}_0 \left(\frac{v\Lambda}{R}\right)^{2-\frac{1}{2}} x + 2\bar{\Delta}_0\bar{\Delta}_3 \left(\frac{v\Lambda}{R}\right)^{2-\frac{1}{2}} (x+z) + 2\bar{\Delta}_3\bar{\Delta}_\perp \left(\frac{v\Lambda}{R}\right)^{2-\frac{1}{2}} (x-z), \quad (\text{B49})$$

$$\frac{d\bar{\Delta}_\perp}{dl} = -\frac{1}{2}\bar{\Delta}_\perp + \bar{\Delta}_0\bar{\Delta}_3 \left(\frac{v\Lambda}{R}\right)^{2-\frac{1}{2}} (x-z) - \bar{\Delta}_0\bar{\Delta}_\perp \left(\frac{v\Lambda}{R}\right)^{2-\frac{1}{2}} (x+z) + 3\bar{\Delta}_3\bar{\Delta}_\perp \left(\frac{v\Lambda}{R}\right)^{2-\frac{1}{2}} (x+z), \quad (\text{B50})$$

$$\begin{aligned} \frac{d\bar{\Delta}_3}{dl} = & -\frac{1}{2}\bar{\Delta}_3 + 2(\bar{\Delta}_0 - 2\bar{\Delta}_\perp + \bar{\Delta}_3)\bar{\Delta}_3 \left(\frac{v\Lambda}{R}\right)^{2-\frac{1}{2}} z \\ & + (\bar{\Delta}_0^2 + 2\bar{\Delta}_\perp^2 + \bar{\Delta}_3^2) \left(\frac{v\Lambda}{R}\right)^{2-\frac{1}{2}} (x+z) + 2\bar{\Delta}_0\bar{\Delta}_\perp \left(\frac{v\Lambda}{R}\right)^{2-\frac{1}{2}} (x-z), \end{aligned} \quad (\text{B51})$$

with $R^2 \equiv m^2 + (v\Lambda)^2$, $\bar{m} \equiv m/R = -\cos[2\phi_2]$, $v\Lambda/R = \sin[2\phi_2]$ and,

$$\bar{\Delta}_\mu \equiv \Delta_\mu \frac{\pi}{4} \frac{(v\Lambda)^{\frac{1}{2}}}{4\pi^2 v^2 b^{\frac{1}{2}}}, \quad x \equiv \frac{1}{\cos[\phi_2]}, \quad y \equiv \cos[\phi_2], \quad z \equiv \cos[3\phi_2]. \quad (\text{B52})$$

The set of equations have two non-trivial fixed points and one trivial fixed points;

$$\text{FP0} : \left(z, \frac{m}{R}, \bar{\Delta}_0, \bar{\Delta}_\perp, \bar{\Delta}_3 \right) = (1, 0, 0, 0, 0.0) \quad (\text{B53})$$

$$\text{FP1} : \left(z, \frac{m}{R}, \bar{\Delta}_0, \bar{\Delta}_\perp, \bar{\Delta}_3 \right) = (1.41, -0.447, 0.137, 0.0128, 0.0440) \quad (\text{B54})$$

$$\text{FP2} : \left(z, \frac{m}{R}, \bar{\Delta}_0, \bar{\Delta}_\perp, \bar{\Delta}_3 \right) = (1.43, -0.753, 0.0, 0.0, 0.376). \quad (\text{B55})$$

Here FP0 and FP1 correspond to FP0 and FP1 in the large- n limit, respectively. The trivial fixed point is a saddle point of the RG flows, around which the linearized

equations take forms of

$$\frac{dm}{dl} = m, \quad \frac{d\bar{\Delta}_\mu}{dl} = -\frac{1}{2}\bar{\Delta}_\mu, \quad (\text{B56})$$

with $\mu = 0, \perp, 3$. The fixed point FP1 is a saddle point,

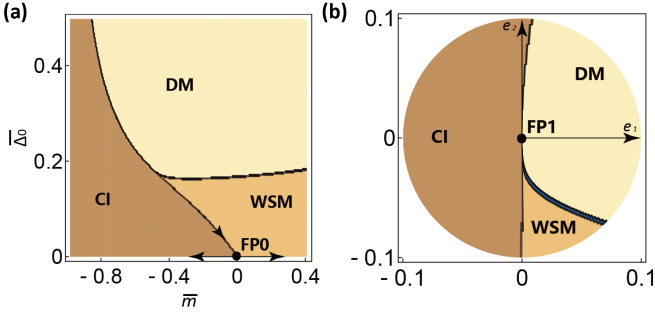


FIG. 9. (color online) (a) Phase diagram in the $\bar{\Delta}_0$ - \bar{m} plane determined by the RG equations in the case of $n = 2$. (b) Phase diagram around FP1 in a plane subtended by e_1 and e_2 .

which determines the quantum multicriticality among the DM, WSM, and CI phases. Namely, linearized RG equations around FP1 have two linear-independent directions in a four-dimensional parameter space, m - $\bar{\Delta}_0$ - $\bar{\Delta}_1$ - $\bar{\Delta}_3$ space, along which the RG flow always goes into FP1, and has two other linear-independent directions, along which the RG flow always runs away from FP1. Let us call the latter two directions as e_1 and e_2 . These two belong to eigenvalues $\lambda_1 = +1.14 \dots$ and $\lambda_2 = +0.287 \dots$, respectively. When an initial parameter set of $(m, \bar{\Delta}_0, \bar{\Delta}_1, \bar{\Delta}_3)$ slightly deviates from FP1 along $\pm e_1$, the corresponding RG flow goes to the DM and CI phase fixed points, respectively (see Fig. 9(b)). When an initial set deviates from FP1 along $\pm e_2$, the flow goes to CI and WSM phase fixed points, respectively (see Fig. 9(b)). FP2 is an unstable point of the RG flow; linearized RG equations around FP2 have four linear-independent directions, along which the RG flow always runs away from FP2.

Appendix C: Density of States and Diffusion Constant Scaling in Crossover Regimes

A scaling theory of the density of states (DOS) and diffusion constant proposed by Kobayashi et.al. [15] is characterized by dynamical exponent z , critical exponent ν and spatial dimension d . As above, there exist a number of fixed points in a phase diagram of disordered Weyl semimetal. Every fixed point has different critical and dynamical exponents. To see how these scalings change along a quantum critical line which connects two fixed points with different exponents, let us argue the DOS and diffusion constant scalings in the framework of the renormalization group language.

1. DOS scaling around Saddle-Point Fixed Point

Consider first a quantum phase transition between two phases, where a finite density of states at $\mathcal{E} = 0$ in one

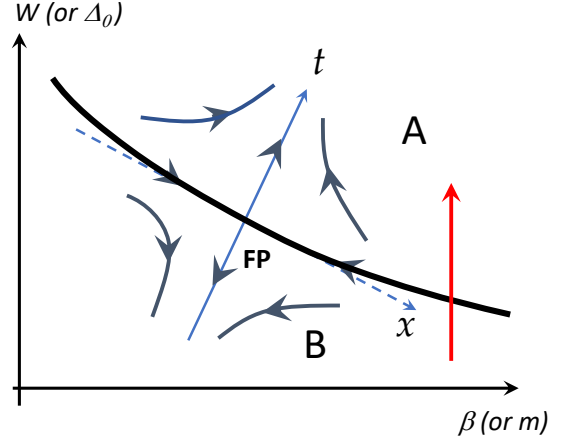


FIG. 10. (color online) Schematic RG phase diagram around a saddle-point fixed point with one relevant scaling variable t and one irrelevant scaling variable x in a two-dimensional parameter space subtended by microscopic parameters such as W and β . The bold solid line is a phase boundary between A phase and B phase. The fixed point controls critical properties of the continuous phase transition between these two.

of the two phases or in both of these two phases become zero or infinite at the critical point. Suppose that critical properties of this continuous phase transition is controlled by a saddle-point fixed point, which has one relevant scaling variable t and one irrelevant scaling variable x (see Fig. 10). Around the fixed point, these two scaling variables, single-particle energy and spatial length are scaled as follows,

$$t' = b^{-y_t} t, \quad (C1)$$

$$x' = b^{-y_x} x = b^{|y_x|} x, \quad (C2)$$

$$\xi' = b \xi, \quad (C3)$$

$$\mathcal{E}' = b^{-z} \mathcal{E}, \quad (C4)$$

with $y_t > 0$ and $y_x < 0$. Variables with prime in the left hand side are those after a renormalization, and those without prime in the right hand side are variables before the renormalization; $b = e^{-dl} < 1$. When the scaling is spatially isotropic, a volume is scaled by b^d (d is a spatial dimension). Thereby, a total number of single-particle states below a given energy \mathcal{E} per unit volume $N(\mathcal{E}, t, x)$ is scaled by b^{-d} under the renormalization;

$$N'(\mathcal{E}', t', x') = b^{-d} N(\mathcal{E}, t, x).$$

Taking a derivative with respect to the energy \mathcal{E} , we obtain a scaling of the density of states under the renormalization,

$$b^{d-z} \rho'(b^{-z} \mathcal{E}, b^{-y_t} t, b^{-y_x} x) = \rho(\mathcal{E}, t, x), \quad (C5)$$

with $\rho \equiv dN/d\mathcal{E}$.

To address ourselves to a scaling property of DOS near a critical point, take t to be very small while x is

not. Suppose that we renormalize many times, such that $b^{-y_t}t = 1$ ($b < 1$, $y_t > 0$). Solving b in favor for t , we have,

$$\rho(\mathcal{E}, t, x) = t^{-\frac{z-d}{y_t}} \rho'(t^{-\frac{z}{y_t}} \mathcal{E}, 1, t^{\frac{|y_x|}{y_t}} x).$$

t is sufficient small, so that the third argument is tiny. Thus, we have,

$$\begin{aligned} \rho(\mathcal{E}, t, x) &\simeq t^{-\frac{z-d}{y_t}} \rho'(t^{-\frac{z}{y_t}} \mathcal{E}, 1, 0) \\ &\equiv t^{-\frac{z-d}{y_t}} \Psi(t^{-\frac{z}{y_t}} \mathcal{E}). \end{aligned} \quad (\text{C6})$$

Noting that $\xi = at^{-\frac{1}{y_t}}$ (where a is an atomic length scale), we reach the same DOS scaling by Kobayashi et al. [15],

$$\rho(\mathcal{E}, t, x) = \xi^{z-d} \Psi(\xi^z \mathcal{E}). \quad (\text{C7})$$

In the presence of finite strength of the irrelevant scaling variable ($x \neq 0$), the above DOS scaling is valid in a critical regime specified by

$$x \ll t^{-\frac{|y_x|}{y_t}}. \quad (\text{C8})$$

Our lattice model is characterized by microscopic parameters such as the disorder strength W and an inter-layer coupling strength β . In the two-dimensional parameter space subtended by W and β , the fixed point has one relevant scaling variable t and one irrelevant scaling variable x , both of which are functions of W and β . The phase boundary between the two phases, $W_c(\beta)$, is determined by

$$t(W_c(\beta), \beta) = 0. \quad (\text{C9})$$

For a given β , we can expand $t(W, \beta)$ in small $W - W_c(\beta)$;

$$\begin{aligned} t(W, \beta) &= \left(\frac{\partial t}{\partial W} \right)_{|W=W_c(\beta)} \cdot (W - W_c(\beta)) + \dots \\ &\equiv a(\beta) \cdot (W - W_c(\beta)) + \dots. \end{aligned} \quad (\text{C10})$$

Substituting this expansion into Eq. (C6), we obtain the following scaling form for the density of states as a function of W and \mathcal{E} ,

$$\begin{aligned} \rho(\mathcal{E}, W, \beta) &= (a(\beta)|W - W_c(\beta)|)^{-\frac{z-d}{y_t}} \\ &\times \Phi\left((a(\beta)|W - W_c(\beta)|)^{-\frac{z}{y_t}} \mathcal{E}\right), \end{aligned} \quad (\text{C11})$$

for $W \simeq W_c(\beta)$ and arbitrary β .

2. Diffusion Constant Scaling around the Saddle-Point Fixed Point

Consider next a quantum phase transition between two phases, where a finite diffusion constant at $\mathcal{E} = 0$ in one of the two phases or both phases diverges or vanishes at its transition point. Such a phase transition includes not only disorder-driven semimetal-metal quantum phase

transition in single Weyl node, but also conventional localization-delocalization transition. We suppose that critical properties of this continuous phase transition is controlled by a saddle-point fixed point which has one relevant scaling variable t and one irrelevant scaling variable x (Fig. 13). Around this fixed point, these two variables as well as characteristic length scale ξ and the single-particle energy \mathcal{E} are scaled as in Eqs. (C1-C4). To see scaling properties of the diffusion constant, we begin with a mean-square displacement of single-particle states of energy \mathcal{E} at time s as a function of the two scaling variables;

$$g_r(\mathcal{E}, s, t, x) \equiv \langle \mathbf{r}^2(\mathcal{E}, s, t, x) \rangle. \quad (\text{C12})$$

Under the spatially isotropic scaling, the mean square displacement is normalized by b^2 under the renormalization,

$$b^{-2} g'_r(\mathcal{E}', s', t', x') = g_r(\mathcal{E}, s, t, x) \quad (\text{C13})$$

with $\mathcal{E}' = b^{-z}\mathcal{E}$, $s' = b^z s$, $t' = b^{-y_t}t$, $x' = b^{|y_x|}x$, and $b < 1$. We consider that the system is close to the critical point, such that t is tiny while x is not. Solving b in favor for t with $b^{-y_t}t = 1$, we obtain a universal scaling form for the mean square distance;

$$g_r(\mathcal{E}, s, t, x) = t^{-\frac{2}{y_t}} \Psi_r(t^{-\frac{z}{y_t}} \mathcal{E}, t^{\frac{z}{y_t}} s).$$

Since t is tiny and $y_t > 0$, we Taylor-expand the second argument for arbitrary time s ;

$$g_r(\mathcal{E}, s, t, x) = t^{-\frac{2}{y_t}} f(t^{-\frac{z}{y_t}} \mathcal{E})s + \mathcal{O}(s^2).$$

This gives us a scaling form of the diffusion constant as

$$D(\mathcal{E}, t, x) = t^{-\frac{z-2}{y_t}} f(t^{-\frac{z}{y_t}} \mathcal{E}). \quad (\text{C14})$$

In the parameter space subtended by microscopic parameters such as W and β , the scaling takes a form of

$$\begin{aligned} D(\mathcal{E}, W, \beta) &= (a(\beta)|W - W_c(\beta)|)^{-\frac{z-2}{y_t}} \\ &\times f\left((a(\beta)|W - W_c(\beta)|)^{-\frac{z}{y_t}} \mathcal{E}\right). \end{aligned} \quad (\text{C15})$$

Appendix D: DOS, Diffusion Constant, and Conductivity Scalings around the Quantum Multicritical Point (QMCP)

In the previous section, we have discussed the DOS and diffusion constant scalings around a saddle-point fixed point, which has only one relevant scaling variable and (more than) one irrelevant scaling variables. In this section, we generalize the RG scaling argument into an unstable fixed point which has two relevant scaling variables. Such a fixed point generally plays a role of a quantum multicritical point (QMCP). In the present study, FP1 in Fig. 8 corresponds to this QMCP.

In the next subsection, we first postulate a global RG phase diagram of disordered Weyl semimetal. The RG

phase diagram includes not only the saddle-point fixed point (FP0) and unstable fixed point (FP1), which are derived from the RG analyses of disordered ‘magnetic dipole’ model in the previous section, but also all the other saddle-point fixed points that surround the unstable fixed point. In Appendix. D3, we derive scaling forms of DOS and diffusion constants around and on the QMCP. In Appendices. D4, D5, and D6, we derive scaling forms around all the other saddle-point fixed points that encompass QMCP. Combining these knowledge together and using the Einstein relation, we complete in Table IV DOS, diffusion constant and conductivity scalings around QMCP as well as all the quantum critical lines which branch out from QMCP.

1. postulated Global RG phase diagram

The previous RG analyses of the disordered magnetic-dipole model gives the saddle-point fixed point in the clean limit (FP0) and unstable fixed point at finite disorder strength (FP1). The critical line connecting these two intervenes the insulator phase with finite gap ($m < 0$) and Weyl semimetal phase with a pair of Weyl nodes ($m > 0$). Near the critical line including the two fixed points, the mass term (m) is a relevant scaling variable. When the mass term blows up into a larger value (either positive or negative), the magnetic dipole model is no longer an appropriate low-energy model.

For positively large m , low-energy physics is well described by a single Weyl node model. Previous RG analyses of the disordered single Weyl node model shows the presence of the stable fixed point in the clean limit and a saddle-point fixed point at finite disorder strength. Let us call them FP5 and FP2, respectively. The numerical studies of the LCI model indicate that critical properties of the semimetal-metal quantum phase boundary between DM and WSM phases are controlled by the latter saddle-point (FP2). This indicates a structure of the global RG phase diagram with positive mass term side as in Fig. 12.

For negatively large m , the situation is rather more involved. Our scaling analysis of localization length and DOS in the main paper suggests that there exist two saddle-point fixed points between QMCP at $m = 0$ and the two-dimensional limit with m being negatively infinite. One saddle-point fixed point controls DOS scaling around a transition between CI phase with zero zDOS and CI phase with finite zDOS. Let us call the CI phase with finite zDOS as CI’ phase and the fixed point as FP3 as in Fig. 12. The other saddle-point fixed point controls critical properties around a localization-delocalization transition between CI’ and DM phases, which belongs to conventional 3D unitary class. Let us call this fixed point as FP4 as in Fig. 12. The diffusion constant is always zero in both of the two CI phases as well as the transition point between these two. On the one hand, DOS does not show any critical behaviour at

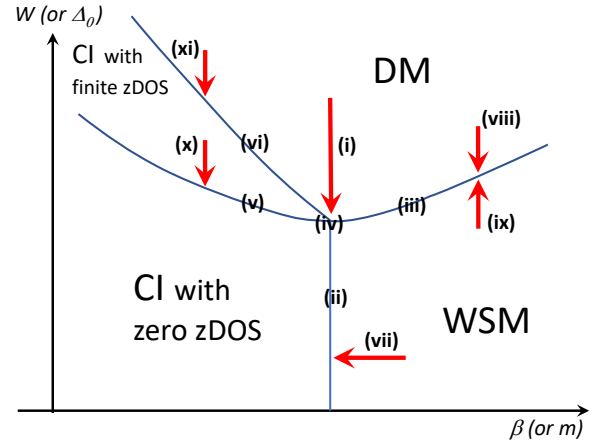


FIG. 11. (color online) Schematic picture of a phase diagram of disordered Weyl semimetal and its critical regions. Roman number (iv) specifies the multicritical point (QMCP). Roman numbers (ii,iii,v,vi) specify quantum critical line between CI and WSM phases, that between WSM and DM phases, that between CI with finite zDOS and CI with zero zDOS, and that between DM and CI with finite zDOS, respectively. Red arrows with roman numbers (i,vii,viii,ix,xi,x) specify a route along which the system approaches quantum critical lines or quantum multicritical point. Corresponding scaling forms of DOS, diffusion constants, effective velocities and life time are described in Table IV.

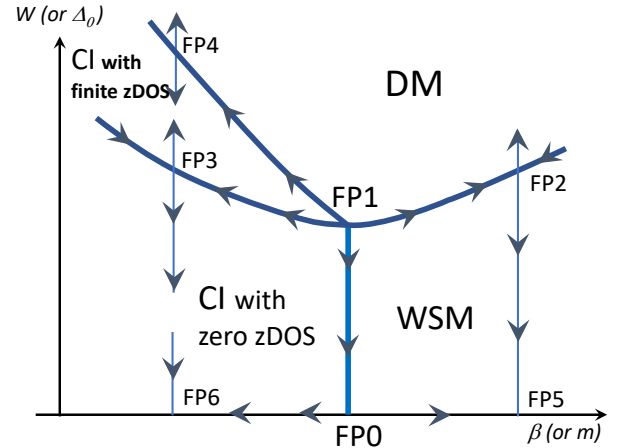


FIG. 12. (color online) Schematic picture of a global RG phase diagram with fixed points. Blue arrow specifies a direction of the RG flow. Bold blue lines are phase boundaries between WSM phase, DM phase, CI phase with zero zDOS and CI phase with finite zDOS.

the transition point between CI’ and DM phases.

	$\rho(0)$ or $\rho(\mathcal{E})$	$D_3(0)$ or $D_3(\mathcal{E})$	$D_{\perp}(0)$ or $D_{\perp}(\mathcal{E})$	$v_3(0)$ or $v_3(\mathcal{E})$	$v_{\perp}(0)$ or $v_{\perp}(\mathcal{E})$	$\tau(0)$ or $\tau(\mathcal{E})$
(i)	$ \delta\bar{\Delta}_0 ^{\frac{2d-1-2z}{2y_{\Delta}}}$	$ \delta\bar{\Delta}_0 ^{\frac{z-1}{y_{\Delta}}}$	$ \delta\bar{\Delta}_0 ^{\frac{z-2}{y_{\Delta}}}$	—	—	$\rho^{-1}(0)$
(ii)	$\mathcal{E}^{d-\frac{3}{2}}$	$\neq 0$	\mathcal{E}^{-1}	$\mathcal{E}^{\frac{1}{2}}$	$\neq 0$	\mathcal{E}^{-1}
(ii)'	$ \delta\bar{\Delta}_0 ^{\frac{2d-1}{2}\frac{1-z}{y_{\Delta}}}\mathcal{E}^{d-\frac{3}{2}}$	$ \delta\bar{\Delta}_0 ^{\frac{z-1}{y_{\Delta}}}$	$ \delta\bar{\Delta}_0 ^{\frac{2(z-1)}{y_{\Delta}}}\mathcal{E}^{-1}$	$ \delta\bar{\Delta}_0 ^{\frac{1}{2}}\frac{z-1}{y_{\Delta}}\mathcal{E}^{\frac{1}{2}}$	$ \delta\bar{\Delta}_0 ^{\frac{z-1}{y_{\Delta}}}$	\mathcal{E}^{-1}
(iii)	$\mathcal{E}^{\frac{d-z'}{z'}}$	$\mathcal{E}^{\frac{z'-2}{z'}}$		$\mathcal{E}^{\frac{z'-1}{z'}}$		\mathcal{E}^{-1}
(iii)'	$ m ^{\frac{2d(z'-z)-z'}{2z'y_m}}\mathcal{E}^{\frac{d-z'}{z'}}$	$ m ^{\frac{2z-z'}{z'y_m}}\mathcal{E}^{\frac{z'-2}{z'}}$	$ m ^{\frac{2(z-z')}{z'y_m}}\mathcal{E}^{\frac{z'-2}{z'}}$	$ m ^{\frac{1}{2}}\frac{2z-z'}{z'y_m}\mathcal{E}^{\frac{z'-1}{z'}}$	$ m ^{\frac{z-z'}{z'y_m}}\mathcal{E}^{\frac{z'-1}{z'}}$	\mathcal{E}^{-1}
(iv)	$\mathcal{E}^{\frac{2d-1-2z}{2z}}$	$\mathcal{E}^{\frac{z-1}{z}}$	$\mathcal{E}^{\frac{z-2}{z}}$	$\mathcal{E}^{\frac{2z-1}{2z}}$	$\mathcal{E}^{\frac{z-1}{z}}$	\mathcal{E}^{-1}
(v)	$\mathcal{E}^{\frac{d-z''}{z''}}$	0		—	—	—
(v)'	$ m ^{\frac{2d(z''-z)-z''}{2z''y_m}}\mathcal{E}^{\frac{d-z''}{z''}}$	0		—	—	—
(vi)	$\neq 0$	$\mathcal{E}^{\frac{z_{3d,u}-2}{z_{3d,u}}}$		—	—	—
(vii)	$ m ^{-\frac{1}{2}}\mathcal{E}^{d-1}$	$ m ^{d-1}\mathcal{E}^{-(d-1)}$	$ m ^{d-2}\mathcal{E}^{-(d-1)}$	$ m ^{\frac{1}{2}}$	$\neq 0$	$m^{d-2}\mathcal{E}^{-(d-1)}$
(viii)	$ \delta\bar{\Delta}_0 ^{\frac{d-z'}{y_{\Delta}}}$	$ \delta\bar{\Delta}_0 ^{\frac{z'-2}{y_{\Delta}}}$		—	—	$\rho^{-1}(0)$
(ix)	$ \delta\bar{\Delta}_0 ^{-\frac{dz'-d}{y_{\Delta}}}\mathcal{E}^{d-1}$	$ \delta\bar{\Delta}_0 ^{\frac{dz'-2}{y_{\Delta}}}\mathcal{E}^{-(d-1)}$		$ \delta\bar{\Delta}_0 ^{\frac{z'-1}{y_{\Delta}}}$		$ \delta\bar{\Delta}_0 ^{\frac{z'(d-2)}{y_{\Delta}}}\mathcal{E}^{-(d-1)}$
(x)	$ \delta\bar{\Delta}_0 ^{\frac{d-z''}{y_{\Delta}}}$	0		—	—	—
(xi)	$\neq 0$	$ \delta\bar{\Delta}_0 ^{\frac{z_{3d,u}-2}{y_{3d,u}}}$		—	—	—

TABLE IV. Scalings of DOS, diffusion constants, effective velocities, and life time near Weyl nodes. \mathcal{E} denotes a single-particle energy. $\rho(0)$ and $\rho(\mathcal{E})$ are DOS for the zero-energy states and for finite (but small) energy states, respectively. $D_{\mu}(0)$ and $D_{\mu}(\mathcal{E})$ are the diffusion constants along the μ direction ($\mu = 3, \perp$) for the zero-energy and the finite energy states, respectively. $v_{\mu}(0)$ and $v_{\mu}(\mathcal{E})$ are the effective velocities along the μ -direction at the zero-energy and finite-energy state in the WSM phase or in the boundary between the WSM and CI phases. $\tau(0)$ and $\tau(\mathcal{E})$ are the life times for the zero-energy and finite-energy states. The Roman number such as (i), (ii), \dots in the first column specifies either a route along which the system approaches the quantum multicritical point or quantum critical lines. The routes with the same Roman number are depicted in Fig. 11. In (iv), the system is on the quantum multicritical point. In (ii), (iii), (v) and (vi), the system is on the quantum critical line between CI and WSM phases, that between WSM and DM phases, that between CI and CI' phases, and that between CI' and DM phases, respectively. In (ii)', (iii)' and (v)', the system approaches QMCP along (ii), (iii) and (v), respectively. $\delta\bar{\Delta}_0$ denotes the disorder strength measured from a critical disorder strength of respective phase transitions (see also the text). m denotes the mass term. y_{Δ} , y_m and z are scaling dimensions of the disorder strength $\delta\bar{\Delta}_0$ and the mass term m and the dynamical exponent at the quantum multicritical point (QMCP), respectively. y'_{Δ} and z' are scaling dimension of the disorder strength and dynamical exponent around FP2, respectively. y''_{Δ} and z'' are those for FP3. $y_{3d,u}$ and $z_{3d,u}$ are those for FP4, which belongs to the conventional 3D unitary class. See also Table I.

2. spatially anisotropic scaling in magnetic dipole model

The critical theory described by Eq. (1) at $m = 0$ has a linear dispersion along the in-plane directions, and a quadratic dispersion along the 3-direction. This naturally leads to a spatially anisotropic scaling around the quantum critical line between CI and WSM phases including its two end points (FP0 and FP1),

$$\begin{cases} \xi'_3 = b^{\frac{1}{2}}\xi_3, \\ \xi'_{\perp} = b\xi_{\perp}. \end{cases} \quad (\text{D1})$$

Here ξ_{\perp} and ξ_3 denote characteristic length scales within the in-plane directions and along the 3-direction, respectively. FP1 (QMCP) has two relevant scaling variables, $\delta\bar{\Delta}_0 \equiv \bar{\Delta}_0 - \bar{\Delta}_{0,c}$ and m , which are scaled by respective scaling dimensions, y_{Δ} and y_m ;

$$\begin{cases} \delta\bar{\Delta}'_0 = b^{-y_{\Delta}}\delta\bar{\Delta}_0, \\ m' = b^{-y_m}m. \end{cases} \quad (\text{D2})$$

with $y_{\Delta} > 0$ and $y_m > 0$. FP0 has one relevant scaling variable m and an irrelevant scaling variable $\bar{\Delta}_0$;

$$\begin{cases} \bar{\Delta}'_0 = b^{(d-\frac{5}{2})}\bar{\Delta}_0, \\ m' = b^{-1}m. \end{cases} \quad (\text{D3})$$

3. DOS and Diffusion Constant Scalings around QMCP

Consider first the scalings around FP1 (QMCP). Under the anisotropic scaling, the volume element is scaled by $b^{d-\frac{1}{2}}$ rather than by b^d . Thereby, the DOS after and before the renormalization are related by

$$b^{(d-\frac{1}{2}-z)}\rho'(\mathcal{E}', \delta\bar{\Delta}'_0, m') = \rho(\mathcal{E}, \delta\bar{\Delta}_0, m), \quad (\text{D4})$$

where $\mathcal{E}' = b^{-z}\mathcal{E}$ and z denotes the dynamical exponent at FP1 (QMCP). Besides, the mean square distance along the 3-direction and that within the 1-2 plane are

scaled differently,

$$\begin{cases} b^{-1}g'_3(\mathcal{E}', s', \delta\bar{\Delta}'_0, m') = g_3(\mathcal{E}, s, \delta\bar{\Delta}_0, m), \\ b^{-2}g'_\perp(\mathcal{E}', s', \delta\bar{\Delta}'_0, m') = g_\perp(\mathcal{E}, s, \delta\bar{\Delta}_0, m), \end{cases} \quad (\text{D5})$$

with $s' = b^z s$ and

$$\begin{cases} g_3(\mathcal{E}, s, \delta\bar{\Delta}_0, m) \equiv \langle x_3^2(\mathcal{E}, s, \delta\bar{\Delta}_0, m) \rangle, \\ g_\perp(\mathcal{E}, s, \delta\bar{\Delta}_0, m) \equiv \langle x_\perp^2(\mathcal{E}, s, \delta\bar{\Delta}_0, m) \rangle. \end{cases} \quad (\text{D6})$$

Eqs. (D4), (D5), and (D6) lead to the following two-parameter scalings of DOS and diffusion constants around QMCP. When $\delta\bar{\Delta}_0 = 0$ and the system approaches QMCP ($m = 0$), the scalings for small m and \mathcal{E} are given by

$$\begin{cases} \rho(\mathcal{E}, m) = |m|^{\frac{d-\frac{1}{2}-z}{y_m}} \Psi(|m|^{-\frac{z}{y_m}} \mathcal{E}), \\ D_3(\mathcal{E}, m) = |m|^{\frac{z-1}{y_m}} f_z(|m|^{-\frac{z}{y_m}} \mathcal{E}), \\ D_\perp(\mathcal{E}, m) = |m|^{\frac{z-2}{y_m}} f_\perp(|m|^{-\frac{z}{y_m}} \mathcal{E}), \end{cases} \quad (\text{D7})$$

respectively. When $m = 0$ and the system approaches QMCP ($\delta\bar{\Delta}_0 = 0$), the scalings for small $\delta\bar{\Delta}_0$ and \mathcal{E} are given by

$$\begin{cases} \rho(\mathcal{E}, \delta\bar{\Delta}_0) = |\delta\bar{\Delta}_0|^{\frac{d-\frac{1}{2}-z}{y_\Delta}} \Psi(|\delta\bar{\Delta}_0|^{-\frac{z}{y_\Delta}} \mathcal{E}), \\ D_3(\mathcal{E}, \delta\bar{\Delta}_0) = |\delta\bar{\Delta}_0|^{\frac{z-1}{y_\Delta}} f_z(|\delta\bar{\Delta}_0|^{-\frac{z}{y_\Delta}} \mathcal{E}), \\ D_\perp(\mathcal{E}, \delta\bar{\Delta}_0) = |\delta\bar{\Delta}_0|^{\frac{z-2}{y_\Delta}} f_\perp(|\delta\bar{\Delta}_0|^{-\frac{z}{y_\Delta}} \mathcal{E}). \end{cases} \quad (\text{D8})$$

On QMCP where $\delta\bar{\Delta}_0 = m = 0$, the scalings at small \mathcal{E} are determined only by the dynamical exponent at QMCP;

$$\begin{cases} \rho(\mathcal{E}) \propto |\mathcal{E}|^{\frac{d-\frac{1}{2}-z}{z}}, \\ D_z(\mathcal{E}) \propto |\mathcal{E}|^{\frac{z-1}{z}}, \\ D_\perp(\mathcal{E}) \propto |\mathcal{E}|^{\frac{z-2}{z}}. \end{cases} \quad (\text{D9})$$

When $\delta\bar{\Delta}_0$ is negative and the system approaches the quantum critical line between CI and WSM phases, the scalings for larger m still respect Eq. (D7). Meanwhile, the scalings for smaller m (what we call ‘critical’ regime) are determined by exponents of the saddle-point fixed point in the clean limit (FP0 in Fig. 12: Appendix. D4). A crossover boundary between these two regimes are given by the scaling dimensions of the two relevant scaling variables at FP1;

$$\begin{cases} |\delta\bar{\Delta}_0| \ll B|m|^{\frac{y_\Delta}{y_m}} & : \text{controlled by FP1} \\ |\delta\bar{\Delta}_0| \gg B|m|^{\frac{y_\Delta}{y_m}} & : \text{controlled by FP0} \end{cases} \quad (\text{D10})$$

When m is finite, and the system approaches the quantum critical lines specified by $\delta\bar{\Delta}_0 = 0$, the scalings for larger $\delta\bar{\Delta}_0$ still follow Eq. (D8). Meanwhile, the scalings for smaller $\delta\bar{\Delta}_0$ (‘critical’ regime) are controlled by the saddle-point fixed points such as FP2 ($m > 0$), or FP3 and FP4 ($m < 0$). Crossover boundaries among these regimes are given by,

$$\begin{cases} |m| \ll A|\delta\bar{\Delta}_0|^{\frac{y_m}{y_\Delta}} & : \text{controlled by FP1} \\ |m| \gg A|\delta\bar{\Delta}_0|^{\frac{y_m}{y_\Delta}} & : \text{controlled by FP2, 3, 4} \end{cases} \quad (\text{D11})$$

4. DOS and Diffusion Constant Scalings in CI-WSM branch

Let us consider the scalings of the quantum phase transition between CI and WSM phases. The scalings in the critical regime are controlled by the saddle-point fixed point (FP0) with the anisotropic scaling. Thus, the scaling argument goes in the same way as in Appendix. C; $\bar{\Delta}_0$ corresponds to the irrelevant scaling variable x and m corresponds to the relevant scaling variable t in Appendix. C. Due to the anisotropic scaling, DOS and mean square distances after a renormalization and those before the renormalization are related by

$$\begin{cases} b^{(d-\frac{1}{2}-1)}\rho'(\mathcal{E}', \bar{\Delta}'_0, m') = \rho(\mathcal{E}, \bar{\Delta}_0, m), \\ b^{-1}g'_3(\mathcal{E}', s', \bar{\Delta}'_0, m') = g_3(\mathcal{E}, s, \bar{\Delta}_0, m), \\ b^{-2}g'_\perp(\mathcal{E}', s', \bar{\Delta}'_0, m') = g_\perp(\mathcal{E}, s, \bar{\Delta}_0, m), \end{cases} \quad (\text{D12})$$

with $\mathcal{E}' = b^{-1}\mathcal{E}$, $s' = bs$, $\bar{\Delta}'_0 = b^{d-\frac{5}{2}}\bar{\Delta}_0$, and $m' = b^{-1}m$. The dynamical exponent at FP0 is 1. When m is tiny, DOS and diffusion constants follow universal scaling forms,

$$\begin{cases} \rho(\mathcal{E}, \bar{\Delta}_0, m) = m^{d-\frac{3}{2}}\Psi(m^{-1}\mathcal{E}), \\ D_3(\mathcal{E}, \bar{\Delta}_0, m) = f_3(m^{-1}\mathcal{E}), \\ D_\perp(\mathcal{E}, \bar{\Delta}_0, m) = m^{-1}f_\perp(m^{-1}\mathcal{E}). \end{cases} \quad (\text{D13})$$

Suppose that the system is in the WSM phase ($m > 0$). A low-energy effective electronic band structure comprises of a pair of two Weyl nodes with velocities v_3 and v_\perp (see Eq. (1)). The DOS near the nodes is given by a quadratic function of the energy; $\rho(\mathcal{E}) = v_3^{-1}v_\perp^{-2}|\mathcal{E}|^{d-1}$. The diffusion constants near nodes D_μ ($\mu = 3, \perp$) are given by respective velocities v_μ and a life time around the node $\tau(\mathcal{E})$;

$$D_\mu(\mathcal{E}) = v_\mu^2\tau(\mathcal{E}), \quad (\text{D14})$$

($\mu = 3, \perp$). Note that v_3 depends on the single-particle energy \mathcal{E} . The self-consistent Born analysis relates the life time with an inverse of the DOS [25],

$$\rho(\mathcal{E}) = \frac{2}{\pi\tau(\mathcal{E})\bar{\Delta}_0}. \quad (\text{D15})$$

Thus, the diffusion constants near the Weyl nodes are inversely proportional to a quadratic function of the energy; $D_\mu(\mathcal{E}) \propto |\mathcal{E}|^{-(d-1)}$. Combining these observations with Eq. (D13), we obtain

$$\begin{cases} \rho(\mathcal{E}, \bar{\Delta}_0, m) \propto m^{-\frac{1}{2}}|\mathcal{E}|^{d-1}, \\ D_3(\mathcal{E}, \bar{\Delta}_0, m) \propto m^{(d-1)}|\mathcal{E}|^{-(d-1)}, \\ D_\perp(\mathcal{E}, \bar{\Delta}_0, m) \propto m^{(d-2)}|\mathcal{E}|^{-(d-1)}, \end{cases} \quad (\text{D16})$$

for small m (> 0) and \mathcal{E} . In terms of the Einstein relation, $\sigma_\mu = e^2\rho D_\mu$, we conclude that the zero-energy conductivities reduce to zero toward the quantum critical line between CI and WSM phases with the following exponents;

$$\begin{cases} \sigma_3 \propto m^{d-\frac{3}{2}}, \\ \sigma_\perp \propto m^{d-\frac{3}{2}}. \end{cases} \quad (\text{D17})$$

Both DOS and diffusion constants at finite energy \mathcal{E} are finite even on the critical line ($m = 0$). This requires the universal scaling functions in Eq. (D13) to have asymptotic forms as,

$$\begin{cases} \Psi(x) \propto x^{d-\frac{3}{2}}, \\ f_3(x) \propto x^0, \\ f_\perp(x) \propto x^{-1}, \end{cases} \quad (\text{D18})$$

for large x . In other words, DOS and diffusion constants on the critical line have energy dependences as,

$$\begin{cases} \rho(\mathcal{E}) \propto |\mathcal{E}|^{d-\frac{3}{2}}, \\ D_3(\mathcal{E}) \propto |\mathcal{E}|^0, \\ D_\perp(\mathcal{E}) \propto |\mathcal{E}|^{-1}. \end{cases} \quad (\text{D19})$$

The Einstein relation further gives the energy dependences of the conductivities around the Weyl node as,

$$\begin{cases} \sigma_3(\mathcal{E}) \propto |\mathcal{E}|^{d-\frac{3}{2}}, \\ \sigma_\perp(\mathcal{E}) \propto |\mathcal{E}|^{d-\frac{5}{2}}. \end{cases} \quad (\text{D20})$$

Finally, let us consider that the system approaches the quantum multicritical point (QMCP) along the critical line between CI and WSM phases ($m = 0$). Near QMCP, DOS and diffusion constants have the universal scaling forms given by Eq. (D8). Combining Eqs. (D19) and (D20) with these scaling forms, we obtain;

$$\begin{cases} \rho(\mathcal{E}) \propto |\delta\bar{\Delta}_0|^{\frac{2d-1}{2}\frac{1-z}{y_\Delta}} |\mathcal{E}|^{d-\frac{3}{2}}, \\ D_3(\mathcal{E}) \propto |\delta\bar{\Delta}_0|^{\frac{z-1}{y_\Delta}} |\mathcal{E}|^0, \\ D_\perp(\mathcal{E}) \propto |\delta\bar{\Delta}_0|^{\frac{2(z-1)}{y_\Delta}} |\mathcal{E}|^{-1}, \\ \sigma_3(\mathcal{E}) \propto |\delta\bar{\Delta}_0|^{\frac{2d-3}{2}\frac{1-z}{y_\Delta}} |\mathcal{E}|^{d-\frac{3}{2}}, \\ \sigma_\perp(\mathcal{E}) \propto |\delta\bar{\Delta}_0|^{\frac{2d-5}{2}\frac{1-z}{y_\Delta}} |\mathcal{E}|^{d-\frac{5}{2}}. \end{cases} \quad (\text{D21})$$

Here y_Δ and z are exponents at QMCP.

On closing this subsection, it is noteworthy to comment that, near the quantum phase transition line between CI and WSM phases, the life time near Weyl nodes respect the following universal scaling form,

$$\tau(\mathcal{E}, \bar{\Delta}_0, m) = m^{-1} \Phi(m^{-1}\mathcal{E}). \quad (\text{D22})$$

To derive this, we use the RG argument in Eq. (D15). The form has a different exponent with respect to small m , compared to $\rho^{-1}(\mathcal{E}, \bar{\Delta}_0, m)$ in Eq. (D13). The difference is because, in the WSM phase as well as on the phase boundary between CI and WSM phases, $\bar{\Delta}_0$ in the right hand side of Eq. (D15) goes to zero on the renormalization; $\bar{\Delta}'_0 = b^{d-\frac{5}{2}}\bar{\Delta}_0$. In the WSM phase ($m > 0$), the life time is inversely proportional to \mathcal{E}^{d-1} , so that it behaves as

$$\tau(\mathcal{E}, \delta\bar{\Delta}_0, m) \propto m^{d-2} |\mathcal{E}|^{-(d-1)}, \quad (\text{D23})$$

for small positive m . At the critical point ($m = 0$), the life time is scaled by the finite energy \mathcal{E} as

$$\tau(\mathcal{E}, \delta\bar{\Delta}_0, m = 0) \propto |\mathcal{E}|^{-1}. \quad (\text{D24})$$

5. DOS and Diffusion Constant Scalings in WSM-DM branch

Consider the scalings in the quantum phase transition between WSM and DM phases. The scaling properties in the critical regime are determined by the saddle-point fixed point with the spatially isotropic scaling (FP2 in Fig. 12). Thus, the argument goes exactly in the same way as in Appendix. C, where $\delta\bar{\Delta}_0 \equiv \bar{\Delta}_0 - \bar{\Delta}_{0,c}$ and m correspond to relevant scaling variable t and irrelevant scaling variable x in Appendix. C, respectively and $\bar{\Delta}_{0,c}$ generally depends on m . For small $\delta\bar{\Delta}_0$ and positive m , DOS and diffusion constant respect the following scaling forms;

$$\begin{cases} \rho(\mathcal{E}, \delta\bar{\Delta}_0, m) = |\delta\bar{\Delta}_0|^{-\frac{z'-d}{y'_\Delta}} \Psi(|\delta\bar{\Delta}_0|^{-\frac{z'}{y'_\Delta}} \mathcal{E}), \\ D(\mathcal{E}, \delta\bar{\Delta}_0, m) = |\delta\bar{\Delta}_0|^{-\frac{2-z'}{y'_\Delta}} f(|\delta\bar{\Delta}_0|^{-\frac{z'}{y'_\Delta}} \mathcal{E}). \end{cases} \quad (\text{D25})$$

z' and y'_Δ are dynamical exponent and scaling exponent of the relevant scaling variable $\delta\bar{\Delta}_0$ at the saddle-point fixed point. These exponents have been evaluated both by the renormalization group studies and by simulational studies [10, 12, 15, 19–22, 25, 27, 29, 31]. In DM phase ($\delta\bar{\Delta}_0 > 0$), DOS and diffusion constant are finite at the zero energy;

$$\begin{cases} \rho(\mathcal{E} = 0, \delta\bar{\Delta}_0, m) \propto \delta\bar{\Delta}_0^{-\frac{z'-d}{y'_\Delta}}, \\ D(\mathcal{E} = 0, \delta\bar{\Delta}_0, m) \propto \delta\bar{\Delta}_0^{-\frac{2-z'}{y'_\Delta}}, \\ \sigma(\mathcal{E} = 0, \delta\bar{\Delta}_0, m) \propto \delta\bar{\Delta}_0^{-\frac{2-d}{y'_\Delta}}. \end{cases} \quad (\text{D26})$$

In the WSM phase ($\delta\bar{\Delta}_0 < 0$), DOS and diffusion constant near Weyl nodes behave as $|\mathcal{E}|^{d-1}$ and $|\mathcal{E}|^{-(d-1)}$, respectively; these scaling forms thus reduce to

$$\begin{cases} \rho(\mathcal{E}, \delta\bar{\Delta}_0, m) \propto |\delta\bar{\Delta}_0|^{-\frac{dz'-d}{y'_\Delta}} |\mathcal{E}|^{d-1}, \\ D(\mathcal{E}, \delta\bar{\Delta}_0, m) \propto |\delta\bar{\Delta}_0|^{-\frac{2-dz'}{y'_\Delta}} |\mathcal{E}|^{-(d-1)}, \\ \sigma(\mathcal{E}, \delta\bar{\Delta}_0, m) \propto |\delta\bar{\Delta}_0|^{-\frac{2-d}{y'_\Delta}}, \end{cases} \quad (\text{D27})$$

for small \mathcal{E} and $|\delta\bar{\Delta}_0|$. Note that, contrary to the previous study [25], the zero-energy conductivity follows the Wegner's relation without any assumption of the dynamical exponent.

On the quantum critical line ($\delta\bar{\Delta}_0 = 0$), both DOS and diffusion constant take finite values at a finite energy \mathcal{E} . This requirement in combination with the universal scaling forms Eq. (D25) tells us how the DOS, diffusion constant and conductivity on the critical line are scaled with respect to small \mathcal{E} ;

$$\begin{cases} \rho(\mathcal{E}, \delta\bar{\Delta}_0 = 0, m) \propto |\mathcal{E}|^{\frac{d-z'}{z'}}, \\ D(\mathcal{E}, \delta\bar{\Delta}_0 = 0, m) \propto |\mathcal{E}|^{\frac{z'-2}{z'}}, \\ \sigma(\mathcal{E}, \delta\bar{\Delta}_0 = 0, m) \propto |\mathcal{E}|^{\frac{d-2}{z'}}. \end{cases} \quad (\text{D28})$$

Combining Eq. (D28) with the other universal scaling forms around QMCP (Eq. (D7)), we obtain;

$$\left\{ \begin{array}{l} \rho(\mathcal{E}, \delta\bar{\Delta}_0 = 0, m) \propto m^{\frac{1}{2y_m}} (2d\frac{z'-z}{z'} - 1) |\mathcal{E}|^{\frac{d-z'}{z'}}, \\ D_3(\mathcal{E}, \delta\bar{\Delta}_0 = 0, m) \propto m^{\frac{1}{y_m}} (\frac{2z}{z'} - 1) |\mathcal{E}|^{\frac{z'-2}{z'}}, \\ D_{\perp}(\mathcal{E}, \delta\bar{\Delta}_0 = 0, m) \propto m^{\frac{2}{y_m}} (\frac{z}{z'} - 1) |\mathcal{E}|^{\frac{z'-2}{z'}}, \\ \sigma_3(\mathcal{E}, \delta\bar{\Delta}_0 = 0, m) \propto m^{\frac{1}{y_m}} (d - \frac{z}{z'}(d-2) - \frac{3}{2}) |\mathcal{E}|^{\frac{d-2}{z'}}, \\ \sigma_{\perp}(\mathcal{E}, \delta\bar{\Delta}_0 = 0, m) \propto m^{\frac{1}{y_m}} (d - \frac{z}{z'}(d-2) - \frac{5}{2}) |\mathcal{E}|^{\frac{d-2}{z'}}. \end{array} \right. \quad (\text{D29})$$

for small positive m .

6. DOS Scaling in CI-CI' branch and diffusion constant scaling in CI'-DM branch

DOS around $\mathcal{E} = 0$ shows a universal scaling feature at the transition between CI phase with zero zDOS and CI phase with finite zDOS,

$$\rho(\mathcal{E}, \delta\bar{\Delta}_0, m) = |\delta\bar{\Delta}_0|^{\frac{d-z''}{y''_{\Delta}}} \Psi(|\delta\bar{\Delta}_0|^{-\frac{z''}{y''_{\Delta}}} \mathcal{E}), \quad (\text{D30})$$

with $\delta\bar{\Delta}_0 \equiv \bar{\Delta}_0 - \bar{\Delta}_{0,c,1}$ (see Eq. (C11), $y''_{\Delta} = y_t$ and $z'' = z$). $\bar{\Delta}_{0,c,1}$ is a critical disorder for a transition between CI with zero zDOS and CI with finite zDOS, and it generally depends on the mass term m . z'' and y''_{Δ} are dynamical exponent and scaling dimension of the relevant scaling variable $\delta\bar{\Delta}_0$ at the saddle-point fixed point (FP3 in Fig. 12), respectively. From a single-parameter scaling fit given in Fig. 13, we numerically determine these two exponents as $z'' \simeq 1$, and $y''_{\Delta} \simeq 1$. The zero-energy DOS (zDOS) plays role of an order parameter of the transition; the zDOS behaves as

$$\rho(\mathcal{E} = 0, \delta\bar{\Delta}_0, m) \propto \delta\bar{\Delta}_0^{\frac{d-z''}{y''_{\Delta}}}, \quad (\text{D31})$$

for $\delta\bar{\Delta}_0 > 0$. At the transition point, the zDOS vanishes and DOS has a scaling form as a function of small energy \mathcal{E} ;

$$\rho(\mathcal{E}, \delta\bar{\Delta}_0 = 0, m) \propto |\mathcal{E}|^{\frac{d-z''}{z''}}. \quad (\text{D32})$$

Near QMCP, the other universal scaling forms (Eq. (D7)) endows Eq. (D32) with an additional exponent with respect to small mass term m ;

$$\rho(\mathcal{E}, \delta\bar{\Delta}_0 = 0, m) \propto |m|^{\frac{2d(z''-z)-z''}{2z''y_m}} |\mathcal{E}|^{\frac{d-z''}{z''}}. \quad (\text{D33})$$

Here z and y_m are dynamical exponent and scaling dimension of the mass term at QMCP, respectively.

The diffusion constant near $\mathcal{E} = 0$ also shows a universal scaling at the transition between CI with finite zDOS and DM phases. The scaling form is determined by exponents of the conventional 3D unitary fixed point (FP4 in Fig. 12). In terms of dynamical exponent $z_{3d,u}$ and critical exponent $\nu_{3d,u} \equiv 1/y_{3d,u}$ associated with the

fixed point, the diffusion constant around $\mathcal{E} = 0$ is given by a scaling function,

$$D(\mathcal{E}, \delta\bar{\Delta}_0, m) = |\delta\bar{\Delta}_0|^{\frac{z_{3d,u}-2}{y_{3d,u}}} f(|\delta\bar{\Delta}_0|^{-\frac{z_{3d,u}}{y_{3d,u}}} \mathcal{E}), \quad (\text{D34})$$

with $\delta\bar{\Delta}_0 \equiv \bar{\Delta}_0 - \bar{\Delta}_{0,c,2}$. $\bar{\Delta}_{0,c,2}$ denotes a critical disorder strength for the localization-delocalization transition between CI with finite zDOS and DM phases. The zero-energy DOS takes a finite value at the transition point, $\bar{\Delta}_0 = \bar{\Delta}_{0,c,2} > \bar{\Delta}_{0,c,1}$, so that the DOS scaling (Eq. (C6)) generally leads to $z_{3d,u} = d = 3$.

For DM phase side ($\delta\bar{\Delta}_0 > 0$), the diffusion constant at the zero energy evolves continuously from the transition point;

$$D(\mathcal{E} = 0, \delta\bar{\Delta}_0, m) \propto \delta\bar{\Delta}_0^{\frac{z_{3d,u}-2}{y_{3d,u}}}. \quad (\text{D35})$$

At the critical point ($\delta\bar{\Delta}_0 = 0$), the diffusion constant evolves continuously from the zero energy;

$$D(\mathcal{E}, \delta\bar{\Delta}_0 = 0, m) \propto |\mathcal{E}|^{\frac{z_{3d,u}-2}{z_{3d,u}}}. \quad (\text{D36})$$

Combining Eq. (D36) with the other universal scalings around QMCP (Eq. (D7)), we obtain

$$\left\{ \begin{array}{l} D_3(\mathcal{E}, \delta\bar{\Delta}_0 = 0, m) \propto |m|^{\frac{1}{y_m}} (\frac{2z}{z_{3d,u}} - 1) |\mathcal{E}|^{\frac{z_{3d,u}-2}{z_{3d,u}}} \\ D_{\perp}(\mathcal{E}, \delta\bar{\Delta}_0 = 0, m) \propto |m|^{\frac{2}{y_m}} (\frac{z}{z_{3d,u}} - 1) |\mathcal{E}|^{\frac{z_{3d,u}-2}{z_{3d,u}}}, \end{array} \right. \quad (\text{D37})$$

for small mass term (m). The Einstein relation gives the same scalings for the conductivities as Eq. (D37).

Appendix E: polynomial fitting of CI'-DM branch

For those data points in Fig. 2, the polynomial fitting results give $W_c = 2.21$, while we could see by eye that the intersection of curves with different L occur at $W_c = 2.27$ in Fig. 2. Fig. 14(a) is an enlarged figure of Fig. 2. From this, one can see that the intersection of curves with larger size moves in the direction of smaller W , being consistent with the polynomial fitting result ($W_c = 2.21$).

A convergence of the polynomial fitting results with $(m_1, m_2, n_1, n_2) = (2, 0, 3, 1)$ for the data points in Fig. 2 is demonstrated in Fig. 14(b). The figure shows a ratio between the 3rd order term and a sum of the lower order terms:

$$\eta \equiv \frac{a_{3,0}\phi_1^3}{a_{0,0} + a_{1,0}\phi_1 + a_{2,0}\phi_1^2}. \quad (\text{E1})$$

One can see that the ratio is already tiny (below 8%) near the critical disorder W_c ($2.1 < W < 2.4$). This verifies the polynomial fitting with $(m_1, m_2, n_1, n_2) = (2, 0, 3, 1)$.

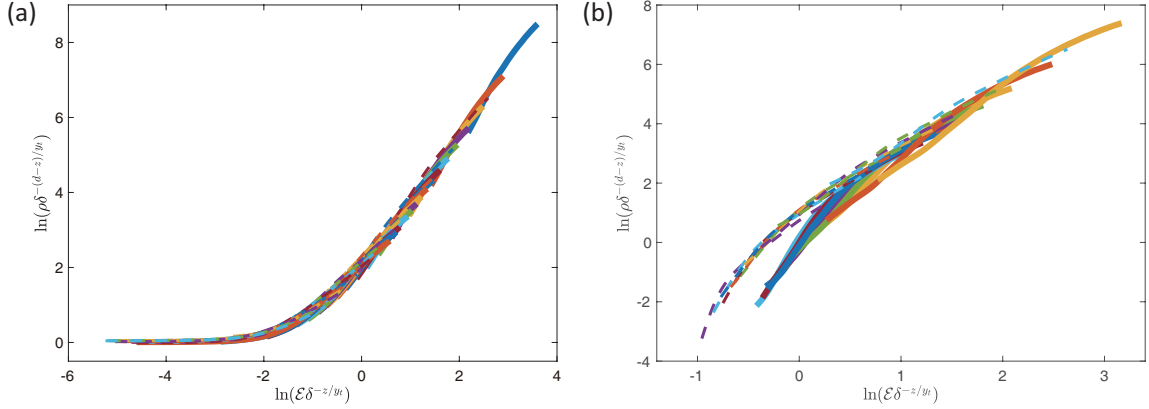


FIG. 13. (color online) Single-parameter scaling of the density of states for $\beta = 0.2$ (solid lines) and $\beta = 0.3$ (dotted lines) for different disorder strength W near the transition point between CI phase with zero zDOS and CI phase with finite zDOS; (a) $W > W_{c,1}$ ($\delta\bar{\Delta}_0 > 0$) (b) $W < W_{c,1}$ ($\delta\bar{\Delta}_0 < 0$). Only those data points with $\rho(\mathcal{E}) > 0.008(0.004)$ are used for the plot for $\beta = 0.2(0.3)$ in (a) and $\rho(\mathcal{E}) > 0.001$ for (b). We use Eq. (C11) for the scaling fit with $(d-z)/y_t = 2$, $z/y_t = 1$ and $\delta \equiv |W - W_{c,1}|/W_{c,1}$. In the fitting for $\beta = 0.2$ and $\beta = 0.3$, we use the same $a(\beta)$ in Eq. (C11). For the CI with finite energy gap, Fig.13 (b), the data streams for $\beta = 0.3$ and those for $\beta = 0.2$ deviate from each other especially when $\mathcal{E}\delta^{-z/y_t}$ becomes smaller. These data points are from those single-particle states which are proximate (and greater than) the energy gap Δ . We speculate that the deviation results from a non-analytic feature of $\rho(\mathcal{E})$ at $\mathcal{E} = \Delta$, and is rather generic in the side of the CI with finite energy gap.

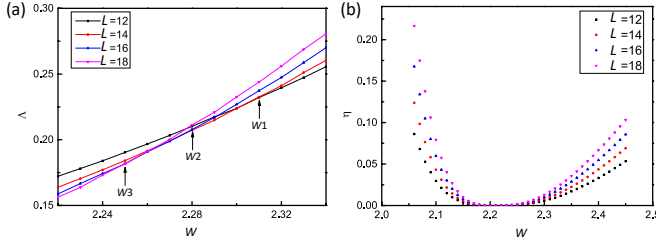


FIG. 14. (color online) (a) Enlarged figure of Fig. 2 around W_c . $W1$, $W2$, $W3$ denote an intersection point between $L=12$, and 14, that between $L = 14$ and 16, that between $L = 16$ and 18, respectively. (b) Ratio between the 3rd order term and a sum of the lower order terms in the polynomial fitting with $(m_1, m_2, n_1, n_2) = (2, 0, 3, 1)$, η given in Eq. (E1), as a function of the disorder strength W for different system size L .

ACKNOWLEDGMENTS

This work (XL, BX, RS) was supported by NBRP of China Grants No. 2014CB920901, No. 2015CB921104, and No. 2017A040215. TO was supported by JSPS KAKENHI Grant No. JP15H03700 and JP17K18763.

-
- [1] S. Murakami, New Journal of Physics **9**, 356 (2007).
 - [2] L. Balents, ‘Weyl electrons kiss’, Physics **4**, 36 (2011).
 - [3] S.-Y. Xu, I. Belopolski, N. Alidoust, M. Neupane, G. Bian, C. Zhang, R. Sankar, G. Chang, Z. Yuan, C.-C. Lee, S.-M. Huang, H. Zheng, J. Ma, D. S. Sanchez, B. K. Wang, F.-C. Bansil, A.; Chou, P. P. Shibayev, H. Lin, S. Jia, and M. Z. Hasan, Science **349**, 613 (2015).
 - [4] B. Q. Lv, H. M. Weng, B. B. Fu, X. P. Wang, J. Miao, Ma, P. Richard, X. C. Huang, L. X. Zhao, G. F. Chen, Z. Fang, X. Dai, T. Qian, and H. Ding, Phys. Rev. X **5**, 031013 (2015).
 - [5] X. Wan, A. M. Turner, A. Vishwanath, and S. Y. Savrasov, Phys. Rev. B **83**, 205101 (2011).
 - [6] H. Weng, C. Fang, Z. Fang, B. A. Bernevig, and X. Dai, Phys. Rev. X **5**, 011029 (2015).
 - [7] X. Huang, L. Zhao, Y. Long, P. Wang, C. Chen, Z. Yang, H. Liang, M. Xue, H. Weng, Z. Fang, X. Dai, and G. Chen, Phys. Rev. X **5**, 031023 (2015).
 - [8] A. A. Burkov and L. Balents, Phys. Rev. Lett. **107**, 127205 (2011).
 - [9] M. Vazifeh and M. Franz, Phys. Rev. Lett. **111**, 027201 (2013).
 - [10] E. Fradkin, Phys. Rev. B **33**, 3263 (1986).
 - [11] R. Shindou and S. Murakami, Physical Review B **79**, 045321 (2009).
 - [12] P. Goswami and S. Chakravarty, Phys. Rev. Lett. **107**,

- 196803 (2011).
- [13] S. Ryu and K. Nomura, *Physical Review B* **85**, 155138 (2012).
- [14] K. Kobayashi, T. Ohtsuki, and K.-I. Imura, *Phys. Rev. Lett.* **110**, 236803 (2013).
- [15] K. Kobayashi, T. Ohtsuki, K.-I. Imura, and I. F. Herbut, *Phys. Rev. Lett.* **112**, 016402 (2014).
- [16] Y. Ominato and M. Koshino, *Phys. Rev. B* **89**, 054202 (2014).
- [17] R. Nandkishore, D. A. Huse, and S. L. Sondhi, *Phys. Rev. B* **89**, 245110 (2014).
- [18] B. Sbierski, G. Pohl, E. J. Bergholtz, and P. W. Brouwer, *Phys. Rev. Lett.* **113**, 026602 (2014).
- [19] B. Roy and S. Das Sarma, *Phys. Rev. B* **90**, 241112 (2014).
- [20] S. V. Syzranov, V. Gurarie, and L. Radzihovsky, *Phys. Rev. B* **91**, 035133 (2015).
- [21] S. V. Syzranov, L. Radzihovsky, and V. Gurarie, *Phys. Rev. Lett.* **114**, 166601 (2015).
- [22] J. H. Pixley, P. Goswami, and S. Das Sarma, *Phys. Rev. Lett.* **115**, 076601 (2015).
- [23] B. Sbierski, E. J. Bergholtz, and P. W. Brouwer, *Phys. Rev. B* **92**, 115145 (2015).
- [24] C.-Z. Chen, J. Song, H. Jiang, Q.-f. Sun, Z. Wang, and X. C. Xie, *Phys. Rev. Lett.* **115**, 246603 (2015).
- [25] S. Liu, T. Ohtsuki, and R. Shindou, *Phys. Rev. Lett.* **116**, 066401 (2016).
- [26] H. Shapourian and T. L. Hughes, *Phys. Rev. B* **93**, 075108 (2016).
- [27] S. Bera, J. D. Sau, and B. Roy, *Phys. Rev. B* **93**, 075108 (2016).
- [28] B. Roy and S. Das Sarma, *Phys. Rev. B* **93**, 119911 (2016).
- [29] S. V. Syzranov, P. M. Ostrovsky, L. Radzihovsky, and V. Gurarie, *Phys. Rev. B* **93**, 155113 (2016).
- [30] J. H. Pixley, D. A. Huse, and S. Das Sarma, *Phys. Rev. X* **6**, 021042 (2016).
- [31] B. Roy, R.-J. Slager, and V. Juricic, *arXiv:1610.08973* (2016).
- [32] Y. Su, X. S. Wang, and X. R. Wang, *arXiv:1701.00905* (2017).
- [33] K. Slevin and T. Ohtsuki, *Phys. Rev. Lett.* **78**, 4083 (1997).
- [34] T. Kawarabayashi, B. Kramer, and T. Ohtsuki, *Phys. Rev. B* **57**, 11842 (1998).
- [35] K. Slevin and T. Ohtsuki, *Journal of the Physical Society of Japan* **85**, 104712 (2016).
- [36] S. Hikami, A. I. Larkin, and Y. Nagaoka, *Progress of Theoretical Physics* **63**, 707 (1980).
- [37] K. B. Efetov, A. I. Larkin, and D. E. Khmel'nitsukii, *Soviet Phys. JETP* **52**, 568 (1980).
- [38] F. Evers and A. D. Mirlin, *Rev. Mod. Phys.* **80**, 1355 (2008).
- [39] A. MacKinnon, and B. Kramers, *Phys. Rev. Lett.* **47**, 1546 (1981).
- [40] J. L. Pichard and G. Sarma, *J. Phys.* **C14**, L127 (1981).
- [41] K. Slevin and T. Ohtsuki, *Phys. Rev. Lett.* **82**, 382 (1999).
- [42] K. Slevin and T. Ohtsuki, *New Journal of Physics* **16**, 015012 (2014).
- [43] K. Slevin, T. Ohtsuki, and T. Kawarabayashi, *Phys. Rev. Lett.* **84**, 3915 (2000).
- [44] A. Weiße, G. Wellein, A. Alvermann, and H. Fehske, *Rev. Mod. Phys.* **78**, 275 (2006).
- [45] Altland, Alexander and Simons, Ben, *Condensed Matter Field Theory* (2010, Cambridge University Press).
- [46] K. Kajita, Y. Nishio, N. Tajima, Y. Suzumura, and A. Kobayashi, *Journal of the Physical Society of Japan*, **83**, 072002 (2014).
- [47] A. Kobayashi, S. Katayama, and Y. Suzumura, *Sci. Technol. Adv. Mater.* **10**, 023309 (2009).
- [48] K. Kajita, N. Tajima, A. Ebina-Tajima, and Y. Nishio, *Synth. Met.* **133**, 95 (2003).
- [49] A. Kobayashi, S. Katayama, Y. Suzumura, and H. Fukuyama, *Journal of the Physical Society of Japan*, **76**, 034711 (2007).
- [50] H. Kino, and T. Miyazaki, *Journal of the Physical Society of Japan*, **75**, 034704 (2006).
- [51] E. P. Wigner and J. von Neuman, *Phys. Z.* **30**, 467 (1929).